# Durability of Aluminum-Copper Laser Welds for EV Battery Applications

by

Andrew (Byung Min) Ko

A thesis

presented to the University of Waterloo

in fulfillment of the

thesis requirement for the degree of

Master of Applied Science

in

Mechanical and Mechatronics Engineering

Waterloo, Ontario, Canada, 2024

© Andrew (Byung Min) Ko 2024

## Author’s Declaration

I hereby declare that I am the sole author of this thesis. This is a true copy of the thesis, including any required final revisions, as accepted by my examiners.

I understand that my thesis may be made electronically available to the public.

# Abstract

Battery packs in electric vehicles (EVs) are typically composed of lithium-ion cells with aluminum and copper as the positive and negative terminals, respectively. These terminals are interconnected in series through conductive tabs to deliver sufficient power output for EV operation. However, joining thin, dissimilar materials like aluminum and copper, each with unique thermo-mechanical and reflectivity characteristics, presents considerable challenges. Among the available joining techniques, laser welding stands out as as a promising method due to its high precision, minimal heat input, and capacity to achieve low electrical contact resistance and high mechanical strength. Additionally, laser welding can effectively limit the formation of brittle intermetallic compounds, which are common in dissimilar metal joints.

This thesis investigates the feasibility of laser welding thin aluminum and copper sheets for use in electric vehicle (EV) battery packs, with a focus on understanding both the quasi-static and fatigue behavior of Al-Cu laser weld joints. To address the challenges of dissimilar metal welding, a process window was developed to produce consistent, robust joints using laser spot sizes of 0.6 mm and 0.3 mm. Through parametric optimization, an optimal combination of laser welding parameters was identified to maximize tensile shear strength and joint reliability. Microstructural analysis revealed the presence of two primary brittle intermetallic phases, Al + θ-$Al_2Cu$ and θ-$Al_2Cu$, at the weld interface.

Mechanical testing of cross-tension specimens under quasi-static and fatigue loading conditions was conducted, particularly in shear-dominant orientations of 90° and 67.5°. As anticipated, specimens tested at the $90^o$ loading orientation generally exhibited a longer fatigue life under the same or similar load levels. Fractographic analysis showed that fatigue cracks typically initiated on the copper side of the weld interface, often at sites of weld porosity or at sharp notches where intermetallic compounds were prevalent. These regions acted as stress concentrators, influencing the crack initiation and propagation mechanisms.

To assess the fatigue behavior, this study employed nCode Rupp's model to transform load-life data into stress-life plots, effectively consolidating fatigue data and reducing scatter in life predictions. Statistical optimization using the generalized reduced gradient (GRG) method further refined the model, enhancing its precision by minimizing residual error and improving the coefficient of determination. With this approach, the study achieved a robust master curve that accurately predicted fatigue life and a R90C90 design curve for Al-Cu laser welds under shear-dominant loading conditions. Subsequent

fatigue tests verified the reliability of this predictive model, supporting its applicability to real-world EV battery pack environments.

# Acknowledgements

I would like to express my deepest gratitude to Professor Hamid Jahed and Professor Adrian Gerlich for warmly welcoming me into the Fatigue and Stress Analysis Lab (FATSLAB) and the Centre for Advanced Materials Joining (CAMJ). Their invaluable guidance, encouragement, and expertise have been instrumental to my academic growth and the completion of this research.

I also extend my sincere appreciation to The Natural Sciences and Engineering Research Council of Canada (NSERC) Alliance program (ALLRP 568648 – 21) and Mitacs (IT27785) for their financial support, and to our industry partner, Stellantis, for their contributions.

I would like to thank Professor Gryguc for his support and to Alan Woo, my colleague and friend, for putting a tremendous amount of effort and time into this work.

Finally, I extend my heartful thanks to my family and my girlfriend for their constant encouragement, understanding, and emotional support throughout my journey.

# Table of Contents

Author's Declaration ..... ii

Abstract ..... iii

Acknowledgements ..... v

List of Figures ..... ix

List of Tables ..... xii

Chapter 1 Introduction ..... 1

1.1 Background ..... 1

1.2 Motivation ..... 1

1.3 Objective ..... 2

1.4 Outline ..... 3

Chapter 2 Background and Literature Review ..... 4

2.1 EV Battery Cell Terminal Connections ..... 4

2.2 Laser Welding ..... 6

2.3 Intermetallic Compounds ..... 7

2.4 Al-Cu Laser Weld Quasi-Static and Cyclic Experimental Work ..... 10

2.5 Fatigue Life Prediction and Model Development ..... 14

2.5.1 Rupp's Model Application ..... 14

2.5.2 Area Contact Method ..... 15

2.5.3 Forces and Moment Recovery ..... 17

2.5.4 Stress Calculations ..... 18

2.5.5 Statistical Optimization ..... 20

Chapter 3 Laser Weld Characterisation ..... 22

3.1 Laser Welding Process Window and Optimization ..... 22

3.1.1 Experimental Setup ..... 22
3.1.2 Process Window ..... 25
3.1.3 Parameter Optimization ..... 28
3.2 Weld Morphology and Microstructure ..... 31
3.2.1 Experimental Setup ..... 31
3.2.2 Weld Cross Section Micrographs and Microhardness ..... 33
3.2.3 SEM and XRD Analysis ..... 35
Chapter 4 Quasi-Static and Fatigue Characterisation ..... 38
4.1 Experimental Setup ..... 38
4.2 Quasi-Static Behavior ..... 42
4.2.1 Quasi-Static Test Procedure ..... 42
4.2.2 Quasi-Static Experimental Results ..... 43
4.3 Fatigue Behavior ..... 45
4.3.1 Fatigue Test Procedure ..... 45
4.3.2 Fatigue Experimental Results ..... 45
Chapter 5 Fatigue Life Prediction ..... 56
5.1 Rupp's Model Application to Cross-Tension Laser Welded Specimens ..... 56
5.1.1 nCode Rupp's Model Pre-Processing ..... 56
5.1.2 nCode Rupp's Model Post-Processing ..... 59
5.2 Statistical Optimization ..... 65
5.3 Rupp's Model Validation ..... 68
Chapter 6 Conclusions ..... 70
6.1 Thesis Conclusions ..... 70
6.2 Recommendations and Future Work ..... 71

References ..... 72

# List of Figures

Figure 1. Overview of the project breakdown ..... 3
Figure 2. The EV battery pack overview with prismatic cells ..... 5
Figure 3: Schematic of laser welding process (lap configuration) ..... 7
Figure 4: Al-Cu binary phase diagram [22] ..... 8
Figure 5: Schematic of Al-Cu joint interface reaction [18] ..... 8
Figure 6: Laser beam oscillation (a) setup schematic (b) laser path input [17] ..... 10
Figure 7: (a) Top view of a laser-welded lap-shear specimen (b) experimental results of the fatigue tests [30] ..... 12
Figure 9: Optical micrographs of the cross sections along the symmetry planes, illustrating examples of failure modes occurring through (a) the aluminum fusion zone and (b) the copper sheet [30] ..... 13
Figure 9: Schematic illustrating the differences between (a) spot weld and (b) circular laser weld ..... 15
Figure 11: Schematic representation of the CBAR method for spot weld modeling [35] ..... 16
Figure 12: Schematic representation of the ACM method [35] ..... 17
Figure 13: Transformation of forces from (a) global coordinates (b) local coordinates and then transferred to (c) the centroids of the top and bottom faces [33] ..... 18
Figure 14: Simplified schematic of a spot weld, illustrating the radial stresses from the inner surfaces of the two sheets [33] ..... 19
Figure 15: Laser welding experimental set-up with fixture ..... 23
Figure 16. Lap shear specimen ..... 24
Figure 17: Tensile testing experimental test setup ..... 24
Figure 17: Example of linear welds: (a) under-welded (b) good weld (c) over-welded ..... 26
Figure 19: Laser welding process window for 0.6 mm spot size ..... 27
Figure 20: Laser welding process window for 0.3 mm spot size ..... 27
Figure 21: Laser welding process window for 0.6 mm and 0.3 mm spot sizes combined ..... 28
Figure 22: Microhardness test experimental setup ..... 32
Figure 23: Setup of (a) optical microscope (b) scanning electron microscope (c) X-ray diffractometers ..... 33
Figure 24. Micrographs of weld seam cross-sections for a joint produced with a normalized laser power of 0.29, a welding speed of 0.5, and a laser spot size of 0.3 mm: (a) unetched sample (b) etched sample, highlighting location microhardness measurements ..... 34

Figure 25. Microhardness measurements conducted on (a) red line (b) blue line (c) green line depicted on Figure 24 ..... 35
Figure 26: SEM images of (a) interface of the weld (b) magnified view of the area highlighted by the red box in part (a) showing selected areas for EDS analysis ..... 36
Figure 27: SEM images of a (a) magnified view of the area highlighted by the red box in part (b) of Figure 26 (b) magnified view of the area highlighted by the red box in part (a) ..... 37
Figure 28. XRD measurements at weld interface ..... 37
Figure 29: Sheet dimensions (in mm) for cross-tension specimen sheet metal joint testing ..... 38
Figure 30: Welding process showing fixture setup, material placement, clamping, welding operation, and final welded assembly ..... 39
Figure 31: Al-Cu laser welded cross-tension coupon where red regions represent test fixture clamped areas ..... 40
Figure 32: Cross-tension test fixture in $90^{o}$ (shear) loading orientation ..... 41
Figure 33: Examples of cross-tension configurations for laser-welded Al-Cu joints with load applied to aluminum sheet ends and copper ends fixed: (a) $90^{0}$ - pure shear (b) $67.5^{o}$ - combined (c) $45^{o}$ - combined (d) $22.5^{o}$ - combined (c) $0^{o}$ - pure tension ..... 41
Figure 34: Instron 8872 with cross-tension fixture ..... 43
Figure 35: Quasi-static test results for $90^{o}$ loading orientation ..... 44
Figure 36: Quasi-static test results for $67.5^{o}$ loading orientation ..... 45
Figure 37: Load-life curve for $90^{o}$ loading orientation with arrow indicating runout data ..... 47
Figure 38: “Eyebrow” failure mode observed in this study (black arrows showing direction of displacement of the aluminum sheet): cracks observed (red arrows showing location of cracks) on (a) aluminum side (b) copper side ..... 48
Figure 39: Schematic representations and micrographs of cross-section (viewed along the dashed lines show in Figure 38) of the welds after interrupted tests at different stages of expected lives in $90^{o}$ loading orientation ..... 49
Figure 40: Load-life curve for $67.5^{o}$ loading orientation with arrow indicating runout data ..... 51
Figure 41: Load-life curve for $90^{o}$ and $67.5^{o}$ loading orientations with arrows indicating runout data 51
Figure 42: Schematic representation and micrographs of cross-section of welds after interrupted test at 70% of expected life in $67.5^{o}$ loading orientation ..... 52

Figure 43: Fracture surface on the copper side of the sample with 393,549 life, showing two types of crack initiation sites: (a) weld porosities (b) weld root notches ..... 53
Figure 44: EDS measurement at a crack initiation region (red arrow indicating direction of measurement) ..... 53
Figure 45: Fracture surface on the copper side of the sample with 272,779 life, showing striations in the crack propagation region ..... 54
Figure 46: Fracture surface on the copper side of the sample with 272,779 life, showing elongated dimples in the final fracture region ..... 55
Figure 47: Schematic representation of the ACM modeling process where red dashed lines represent the distributing coupling elements ..... 57
Figure 48: Schematic representation of (a) al-cu laser weld (b) corresponding ACM model ..... 57
Figure 49: Simplified finite element model of the cross-tension specimen highlighting two clamped areas of the bottom shell element ..... 58
Figure 50: Simplified finite element model of cross-tension specimen highlighting two clamped areas of the upper shell element ..... 58
Figure 51: Simplified finite element model of the cross-tension specimen highlighting load direction for (a) 90$^{o}$ loading orientation corresponding to Figure 32 and part (a) of Figure 33 (b) 67.5$^{o}$ loading orientation corresponding to part (b) of Figure 33 ..... 59
Figure 52: Graphical representation of the rotation matrix calculation ..... 60
Figure 53: Node numbers and coordinate system of the solid element ..... 61
Figure 54: Stress-life plot transferred from load-life using nCode aluminum RSW empirical factors 65
Figure 55: Stress-life plot post statistical optimization ..... 67
Figure 56: Stress-life plot including ±×2 bands (a) pre statistical optimization (b) post statistical optimization ..... 67
Figure 57: Stress-life plot with additional test data for verification ..... 69
Figure 58: Stress-life plot including ±×2 bands with additional test data in (a) 90$^{o}$ loading orientation (b) 67.5$^{o}$ loading orientation ..... 69

# List of Tables

Table 1: Physical properties of aluminum and copper [11] ..... 5
Table 2: Summary of tensile tests conducted on Al-Cu laser lap welds ..... 11
Table 3: nCode typical empirical factors for spot welds in steel ..... 20
Table 4: nCode typical empirical factors for spot welds in aluminum ..... 20
Table 5: Weld evaluation terminologies and descriptions ..... 26
Table 6: Quasi-static tensile test results for 0.6 mm spot size ..... 30
Table 7: Quasi-static tensile test results for 0.3 mm spot size ..... 31
Table 8. EDS analysis of selected areas 1-4 from Figure 26 part (b) ..... 36
Table 9: Test matrix for fatigue tests in 90$^{o}$ loading orientation with load levels determined from maximum load of quasistatic results and r-ratio = 0.1 ..... 46
Table 10: Test matrix for fatigue tests in 67.5$^{o}$ loading orientation with load levels determined from maximum load of quasistatic results and r-ratio = 0.1 ..... 50
Table 11: Calculated forces and moments for each load level ..... 63
Table 12: Calculated structural stresses for each load level ..... 64
Table 13: Optimized empirical factors for Al-Cu laser welds with circular weld seams ..... 68
Table 14: Additional fatigue test results for model verification ..... 68

# Chapter 1
# Introduction

## 1.1 Background

Electric vehicles (EVs) have seen significant advancements in the automotive industry due to their potential to reduce greenhouse gas emissions and decrease reliance on fossil fuels. A critical component of EVs is the battery pack, which demands robust and durable connections to ensure both safety and reliable performance. The reliability of the joints connecting battery cell terminals is critical to battery pack performance. These terminals are typically made of copper and aluminum, chosen for their excellent electrical conductivity, corrosion resistance, and lightweight properties [1].

One of the primary challenges in producing such joints is creating effective and durable joints between dissimilar materials with different thermo-mechanical properties. Joining two different metals like copper and aluminum presents numerous technical difficulties, particularly in terms of ensuring long-term durability and performance under cyclic loading conditions. The differing physical and chemical characteristics of these metals can lead to complications such as the formation of brittle intermetallic compounds (IMC) and residual stresses, which can affect the integrity of the welds [2].

Laser welding has emerged as a promising technique for achieving high-quality joints between these metals. It offers high speed and precision, minimal heat input, and the ability to produce strong, uniform welds with minimal distortion[3]. Despite these advantages, understanding the fatigue behavior of Al-Cu laser weld joints received little attention and remains crucial. Fatigue behavior under operational conditions is a key factor in determining the lifespan and reliability of these joints in EV applications. Thoroughly investigating this aspect will enhance the safety and durability of EV battery packs, supporting the implementation and success of electrification of transportation vehicle, particularly since broken connections can lead to arcing, and pack enclosures are typically hermetically sealed which hinders their repairability.

## 1.2 Motivation

The motivation behind this research is driven by the need to assess and enhance the durability and reliability of EV battery pack joints. As the adoption of electric vehicles continues to grow, the demand for efficient and long-lasting battery connections becomes increasingly important as well. Aluminum-copper laser weld joints are particularly significant because they combine the desirable properties of both metals, leading to potentially superior performance in terms of electrical and thermal conductivity,

and weight reduction. Despite these advantages, the fatigue behavior of these joints under operational conditions is not fully understood, posing a risk to the overall reliability of EV battery systems. By investigating the laser welding of copper-aluminum joints and their fatigue behavior through the establishment of the Rupp's model, this research aims to contribute to the development of more durable and reliable EV battery packs, ultimately supporting the advancement of electric vehicle technology.

## 1.3 Objective

Figure 1 provides a comprehensive overview of the project, highlighting the two primary objectives of the research: to characterise Al-Cu dissimilar laser welds and assess the durability of these joints in EV battery terminal connections. Objective 1 involved examining the welding parameters to establish a process window, optimizing these parameters to improve static strength, and conducting a detailed microstructural analysis of the welds. Objective 2 focused on assessing the mechanical performance of the laser welds, produced during Objective 1, under both quasi-static and cyclic loading conditions. This was achieved through mechanical testing, weld modeling, and generating a master S-N curve to evaluate their durability. Through this characterisation and understanding of fatigue behavior, the study aims to fill the major knowledge gap and accurately assess the durability and predict the fatigue life of Al-Cu laser welded joints. Ultimately, the research aspires to optimize welding techniques and joint designs, thereby significantly enhancing the performance and safety of EV battery systems.

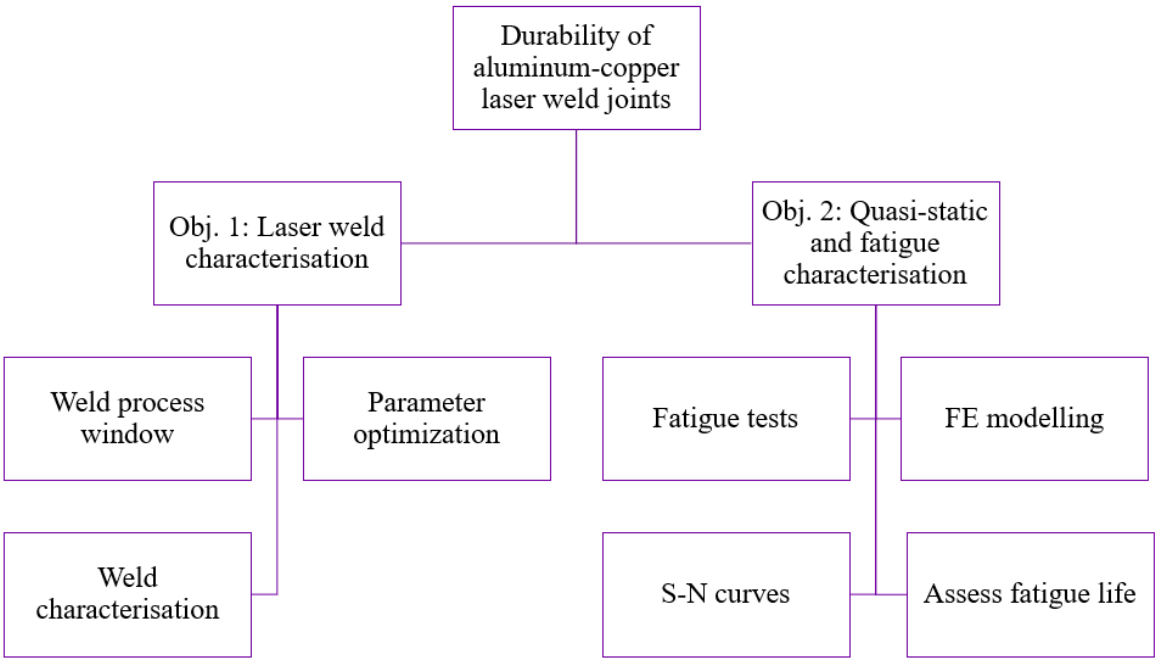



**Figure 1. Overview of the project breakdown**

## 1.4 Outline

Chapter 2 provides an in-depth background on dissimilar laser welding, reviewing previous research on the fundamentals of EV battery cell terminal laser welding. It also explores methods for fatigue life prediction and statistical optimization, highlighting the key advancements and challenges identified by other researchers in this field. Chapter 3 focuses on the laser welding process, detailing the optimization of welding parameters and the characterisation of weld morphology and microstructure. This chapter establishes the process window and examines the influences of various parameters on the quality and properties of the welds. Chapter 4 examines the quasi-static and fatigue behavior of the welds. It covers the preparation of experimental specimens, the testing procedures for both quasi-static and fatigue tests, and presents the resulting data. Chapter 5 discusses the application of nCode Rupp's model to estimate stresses across the welds and to transform the load-life curve into a master stress-life curve. This chapter also explores the enhancement of Rupp's model through statistical optimization, aiming to improve the accuracy and reliability of fatigue life predictions. Chapter 6 summarizes the findings of this study, offering conclusions based on the research outcomes. It also outlines recommendations for industry practices and suggests potential directions for future work to further advance the understanding and application of laser welding in EV battery pack manufacturing.

# Chapter 2
# Background and Literature Review

This chapter documents a review of previous work performed by other researchers in the field of Al-Cu laser welding, weld morphology and microstructure, quasistatic and fatigue experimental results and fatigue life prediction including optimization.

## 2.1 EV Battery Cell Terminal Connections

The battery pack serves as the core of an electric vehicle, consisting of multiple interconnected lithium-ion cells that collectively release the energy needed for the vehicle's operation (see Figure 2). These cells are arranged to optimize both spatial efficiency and performance, ensuring a reliable and high-performing power source. Among the most commonly used cell types for vehicle propulsion are cylindrical, prismatic, and pouch cells [4]. Each type offers distinct advantages, with the selection influenced by factors such as energy density, packing constraints, thermal management, and overall design objectives of the vehicle. The cell terminals are commonly composed of pure aluminum (cathode) and copper (anode), which are interconnected in parallel and series configurations [5], [6]. These interconnections are often made using thin materials, usually ranging between 0.3 mm to 1 mm in thickness, and are commonly executed in lap, fillet, or spot configurations, either directly between the two sheets or through the integration of busbars [7], [8]. The precision in making these connections is crucial, as it not only influences the overall efficiency and power delivery of the battery pack but also plays a critical role in ensuring the safety and long-term durability of the system.

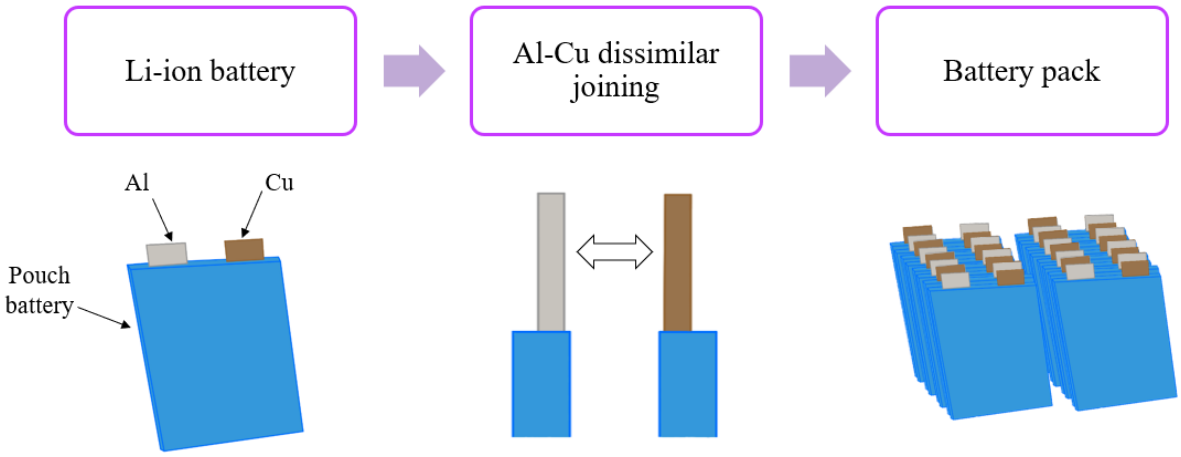



**Figure 2. The EV battery pack overview with prismatic cells**

Manufacturing electrical and structural cell terminal joints introduces several unique challenges, primarily due to the complexity of joining thin, highly conductive, and reflective materials with varying thicknesses. The joining process is further complicated by potential thermal distortion caused by localized heat input. Additionally, ensuring these joints meet durability and fatigue resistance requirements is critical for long-term performance. As highlighted in Table 1, the significant differences in thermo-physical properties of aluminum and copper, such as melting temperatures and thermal conductivities, make it particularly challenging to achieve complete metallurgical bond. These differences often lead to issues like increasing the risk of defects such as cracks, porosities, and incomplete fusion [9]. The formation of hard and brittle intermetallic compounds at the weld interface further complicates matters, as these compounds can reduce both the electrical capacity and structural integrity [10]. To address these challenges, the selection of appropriate joining methods becomes essential.

**Table 1: Physical properties of aluminum and copper** [11]

| Property | Copper | Aluminum |
|---|---|---|
| Density ($g/cm^3$) | 8.91 | 2.71 |
| Melting Temperature ($^oC$) | 1083 | 660 |
| Thermal Conductivity (W/mK) | 390 | 222 |
| Coefficient of Thermal Expansion ($^oC^{-1}$) | $17 \times 10^{-6}$ | $24 \times 10^{-6}$ |
| Specific Heat Capacity (J/kg $^oC$) | 385 | 946 |

## 2.2 Laser Welding

Extensive research has been conducted to evaluate various joining techniques and their performance in electric vehicle battery manufacturing, with the goal of addressing the technical challenges. The findings from these investigations are detailed in references [4], [6], [12], [13], which highlight several commonly employed joining methods in the industry and assess their suitability in battery pack production. Among these, resistance welding, ultrasonic welding, and laser welding were identified as preferred methods for battery pack manufacturing. Resistance welding is cost-effective and fast, but struggles with consistent quality for dissimilar metals and may cause heat damage. Ultrasonic welding, leveraging high-frequency vibrations, excels in joining delicate components and dissimilar metals with minimal heat, but is limited in scalability and joint strength. In contrast, laser welding offers exceptional precision, minimal heat-affected zones, and the ability to join dissimilar metals with superior strength, making it particularly suited for cell terminal welding. Although its initial cost is high, laser welding's scalability, flexibility, and ability to handle complex geometries provide significant advantages over alternative methods.

As shown in Figure 3, laser welding involves joining materials through localized heating, using a highly focused laser beam as the primary energy source [14]. The precision of the laser beam, with its small cross-sectional area and concentrated energy, allows the formation of narrow welds with deep penetration, even at high welding speeds. These characteristics of laser welding allow for a low level of heat to be generated within the assembly, making it particularly advantageous when working with heat sensitive chemicals within the batteries. Most importantly, the laser welding technique minimizes formation of hard intermetallic phases, which are known to degrade electrical conductivity and mechanical strength. As a result, the welded joints exhibit low electrical contact resistance and high structural integrity, making laser welding an ideal solution for electric vehicle battery packs [12].

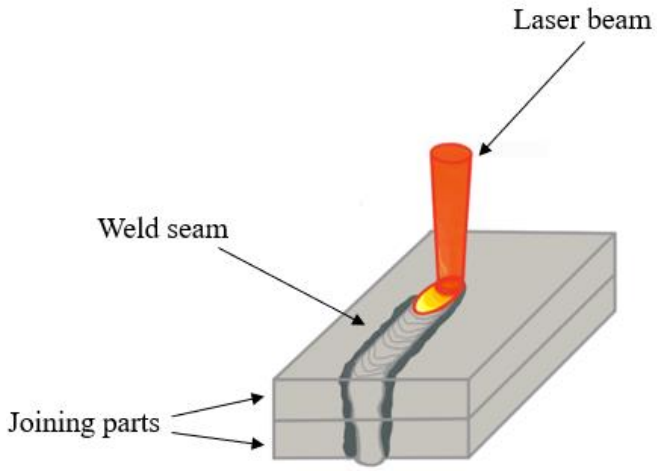



**Figure 3: Schematic of laser welding process (lap configuration)**

## 2.3 Intermetallic Compounds

The Al-Cu equilibrium phase diagram, depicted in Figure 4, illustrates the various intermetallic compounds that can potentially form during the laser welding process. Among the numerous possible intermetallic compounds, previous studies have identified θ-$Al_2Cu$ and Al-Cu eutectic as the most commonly occurring compounds in Al-Cu laser welds [3], [10], [15], [16], [17], [18], [19], [20], [21]. Yan et al. [18] have provided a detailed analysis of the reaction mechanism within the weld metal and interface zone, as outlined in Figure 5. Figure 5(a) and Figure 5(b) show the stirring and convection effects induced by laser irradiation, which result in molten copper and aluminum atoms diffusing into each other. However, rapid solidification following laser exposure limits atomic diffusion, with elemental segregation occurring in the melted zone. As the weld pool solidifies and begins to crystallize, Figure 5(c) shows the formation of Al solid solutions as the temperature drops to around 933.6K. During this cooling process, $Al_2Cu$ IMC begin to precipitate near the Cu solid solution. As the temperature further decreases, the zigzag $Al_2Cu$ IMCs grow into the weld pool, consuming Al and Cu atoms. Figure 5(d) shows the nucleation and growth of the Al-Cu eutectic alloy near the $Al_2Cu$ IMC region at the interface. However, due to the limited diffusion of copper into the weld pool, only a small amount of the Al-Cu eutectic alloy forms within the weld metal. Once the entire weld pool has solidified, the resulting microstructure primarily consists of a large volume of Al solid solution and a small amount of Al-Cu eutectic alloy. At the interface zone, $Al_2Cu$, Al-Cu eutectic alloy, and Cu solid solutions are present.

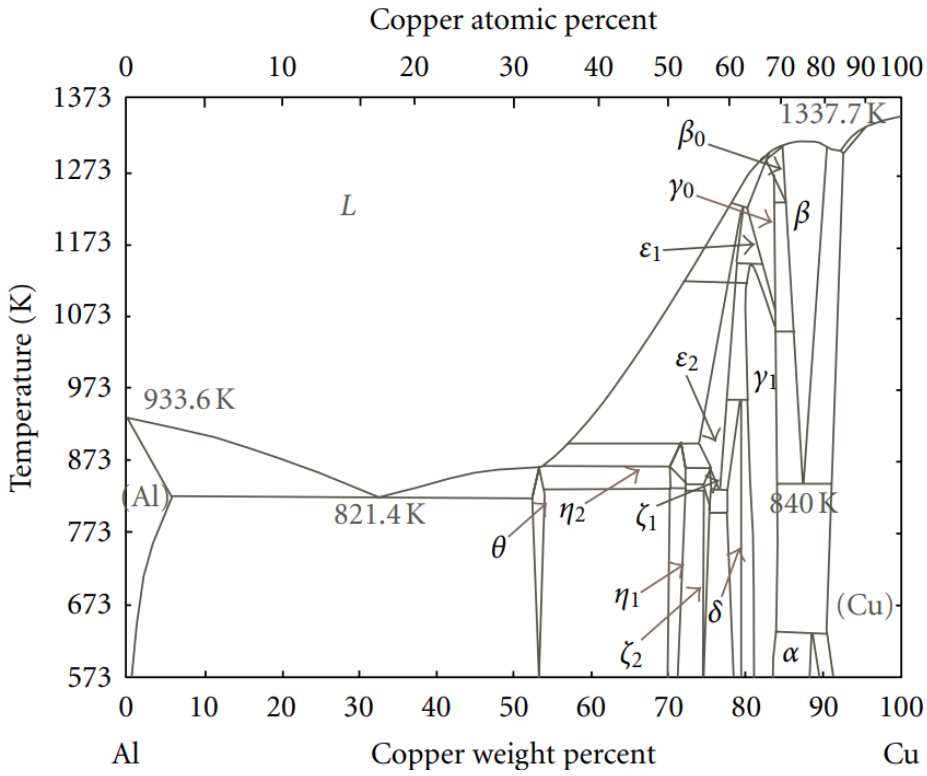



**Figure 4: Al-Cu binary phase diagram** [22]

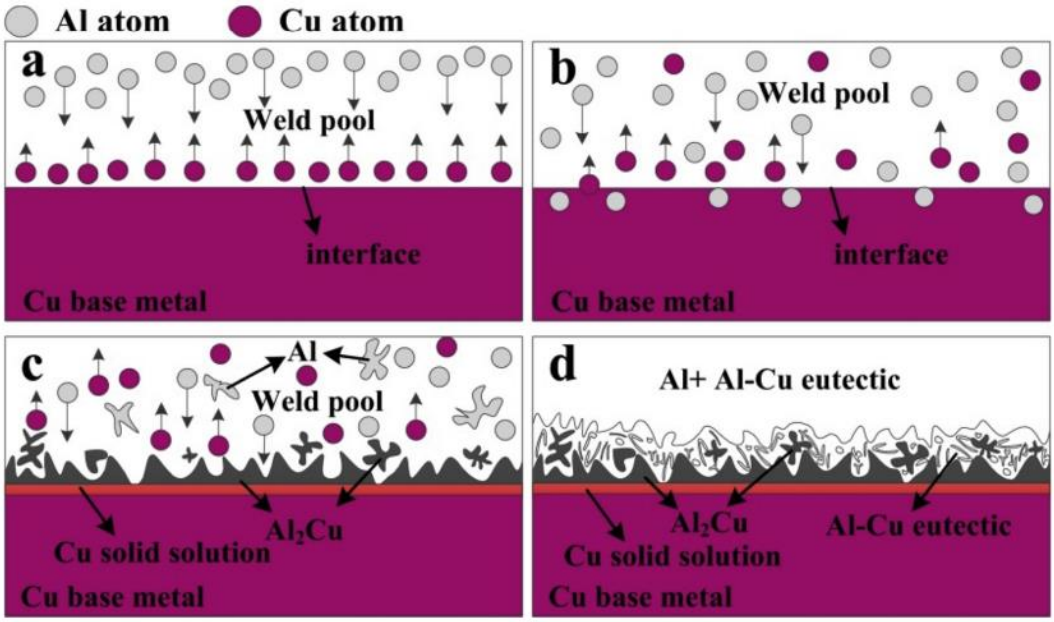



**Figure 5: Schematic of Al-Cu joint interface reaction** [18]

Intermetallic compounds exhibit significantly different mechanical properties compared to pure aluminum and copper, posing challenges in the performance of welded joints. Copper-rich intermetallic compounds, in particular, are characterised by increased hardness due to the rise in ionic and covalent bonding, accompanied by a reduction in metallic bonding [20]. Moreover, the reduction in metallic bonds and the absence of an electron gas result in higher electrical resistivity, which has a detrimental effect on the electrical performance of battery connections [23]. Research led by Schmalen et al. [24] demonstrated a direct relationship between electrical resistance and the thickness of the intermetallic compound layer. Their findings indicate that minimizing the thickness of this layer is crucial for achieving lower electrical resistance in welded joints. This insight highlights the importance of precise control of welding process and fine-tuning of weld parameters to limit the formation of thick intermetallic layers.

Studies have shown that achieving higher welding speed can improve mechanical properties by minimizing the extent of intermetallic compound formation [16]. In addition to optimizing weld parameters, various researchers have explored the use of interlayers made from materials such as tin, nickel, and silver foils, which are placed in-between aluminum and copper to reduce intermetallic phases, thereby enhancing mechanical properties [2], [25], [26]. Recent studies have also suggested the use of spatial beam oscillation, as illustrated in Figure 6, as a method to reduce the thickness of IMC zones [17], [20], [27], [28], [29]. Spatial beam oscillation effectively increases the weld seam width while decreasing the depth. This adjustment minimizes the mixing of aluminum and copper, thus reducing the formation of intermetallic compounds. Furthermore, Jarwitz et al. [29] demonstrated that the copper content in the weld seam is largely dependent on the penetration depth into the lower copper sheet. Their study suggested that this depth decreases as the amplitude of the beam oscillation increases and the frequency decreases.

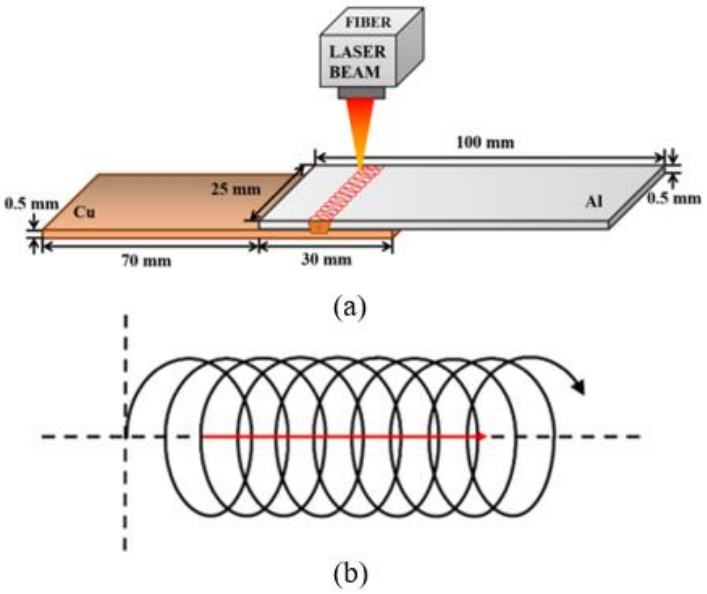



**Figure 6: Laser beam oscillation (a) setup schematic (b) laser path input** [17]

## 2.4 Al-Cu Laser Weld Quasi-Static and Cyclic Experimental Work

Testing of sheet joints is typically conducted at the specimen level to characterise their mechanical behavior before implementing in practical applications. Numerous studies have been conducted to analyze the quasi-static tensile behavior of Al-Cu laser-welded joints, aiming to comprehensively evaluate the joint strength. These investigations are essential for understanding the mechanical properties of these welds, offering critical insights into their potential performance in real-world applications. Table 2 provides a comprehensive summary of prior research on the shear strength of laser-welded joints made from thin sheets of aluminum and copper, utilizing optimized welding parameters. The reviewed studies used aluminum and copper sheets with thicknesses ranging from 0.3 mm to 1.6 mm and weld lengths between 12.7 mm and 30 mm, achieving maximum shear tensile forces between 480 N and 780 N. These results offer valuable benchmarks for the expected joint strengths under specific welding conditions. The findings from these studies not only provide a better understanding of the mechanical performance of Al-Cu laser welds but also serve as a foundation for developing reliable welding process windows.

**Table 2: Summary of tensile tests conducted on Al-Cu laser lap welds**

| Aluminum | Copper | Joint Type | Optimized Laser Parameters | Shear strength | Ref. |
|---|---|---|---|---|---|
| A1050<br>T: 0.3 mm | 99.96% pure Cu<br>T: 0.20 mm | Al-Cu and Cu-Al<br>Weld length: 30 mm | Laser power: 1000 W<br>Welding speed: 10-50 m/min | 480-540 N | [16] |
| A1060<br>T:0.3 mm | T2 Cu<br>TL 0.3 mm | Cu-Al<br>Weld length: 20 mm | Laser power: 1650 W<br>Welding speed: 95 mm/s | 539.52 N | [15] |
| A1100<br>T: 0.8 mm | C1100<br>T: 1.6 mm | Al-Cu<br>Weld length: 12.7 mm<br>Two weld passes | Laser power: 3.0 kW<br>Welding speed: 7.0 m/min | 769 N | [30] |
| 3003-H14<br>T: 0.49 mm | 110-H14<br>T: 0.54 mm | Al-Cu<br>Weld length: 20 mm | Laser power: 460 W<br>Welding speed: 1 m/min | 780 N | [26] |

Unfortunately, there are limited studies focusing on the fatigue behavior of Al-Cu laser-welded joints, an area that is critical for assessing the long-term performance of these connections in real-world applications. The one and only contribution in this area comes from the work of Lai et al., [30] who conducted fatigue tests on laser-welded joints composed of 0.8 mm thick aluminum and 1.6 mm thick copper sheets. The joints were formed using two adjacent 12.7 mm weld passes, resulting in a total weld length of 25.4 mm. The welding process employed a laser power of 3.0 kW and a welding speed of 7.0 m/min, as illustrated in Figure 7(a). The fatigue tests were conducted with a load ratio of R = 0.1 and a test frequency of 10 Hz. These tests were designed to terminate when either the specimens separated or when transverse cracks from the welds became clearly visible. The results, presented in Figure 7(b), show the relationship between load ranges and fatigue life for lap-shear specimens under cyclic loading. A significant degree of scatter in fatigue life was observed at each load level,

emphasizing the difficulty of producing consistent joints and the inherent complexity of fatigue crack initiation and propagation in dissimilar metal welds.

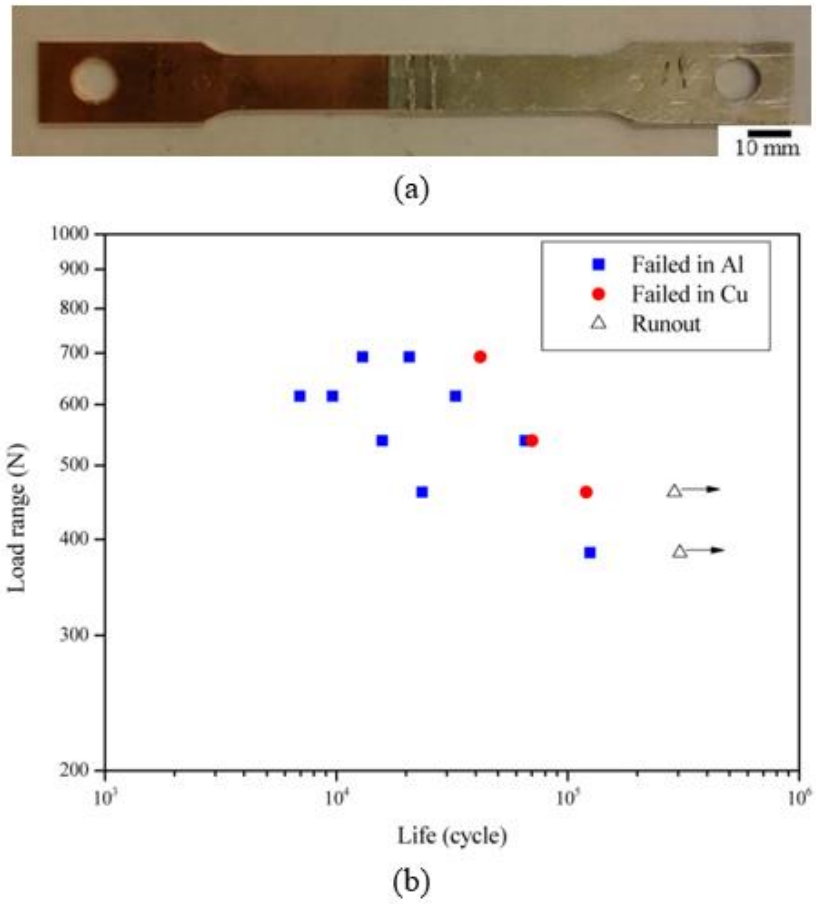



**Figure 7: (a) Top view of a laser-welded lap-shear specimen (b) experimental results of the fatigue tests** [30]

The load-life plot includes two distinct failure modes observed under cyclic loading conditions. Figure 8(a) shows the symmetrical cross-section of a specimen that failed due to a kinked crack within the aluminum fusion zone. In this case, the crack initiated at the interface between the aluminum and copper sheets and propagated into the aluminum fusion zone at an angle close to 90 degrees. The schematic indicates that the interfacial crack developed along the interface between the fusion zone and the copper base metal but did not propagate through the copper sheet. Figure 8(b) depicts the cross-section of a specimen that failed due to an interfacial crack between the fusion zone and the copper base metal. This

interfacial crack propagated along the interface and eventually penetrated the copper sheet, with no kinked cracks observed in or near the aluminum fusion zone.

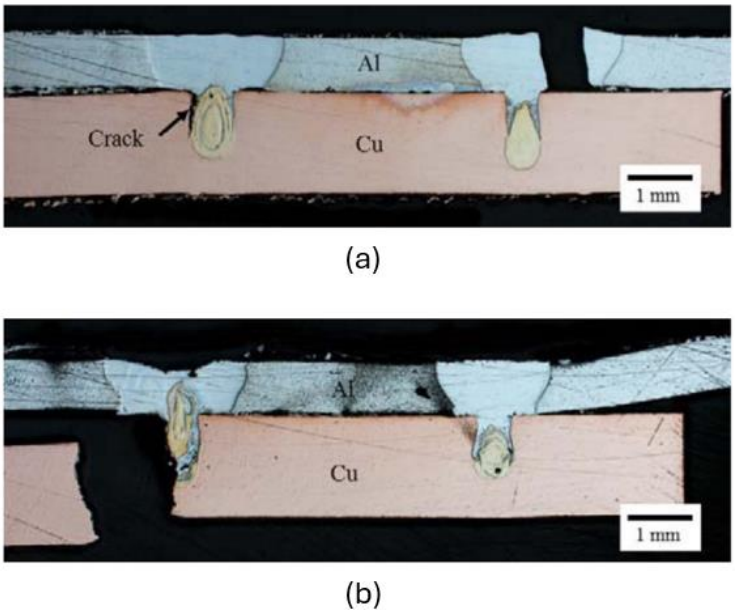



**Figure 8: Optical micrographs of the cross sections along the symmetry planes, illustrating examples of failure modes occurring through (a) the aluminum fusion zone and (b) the copper sheet** [30]

As shown in Figure 7, these failure modes occurred under different load ranges during cyclic loading. Specimens that failed through the copper sheet generally exhibited longer fatigue lives compared to those that failed in the aluminum fusion zone. The author predicted that this phenomenon might be simply due to the greater thickness of the copper sheet, or the superior fatigue strength of the copper compared to the aluminum base metal and fusion zone. However, the predominance of one failure mode over the other under cyclic loading remains unclear. One potential explanation for its variation is the unpredictable nature of weld defects, such as voids created during the welding process, which can lead to varying degrees of stress concentration due to the notch effect. If the notch effect is significant enough to initiate a kinked crack in the aluminum fusion zone, the specimen is more likely to fail in this region. Conversely, if the defect is not significant, the interfacial crack between the fusion zone and the copper sheet may be more likely to lead to failure. The limited research on cyclic experimental work and failure modes underscores the need for further investigation to gain a comprehensive understanding of the fatigue behavior and durability of such joints in practical applications.

## 2.5 Fatigue Life Prediction and Model Development

Fatigue analysis is essential for assessing the durability of any structural system subjected to cyclic loading, as it provides a comprehensive evaluation of its endurance under repeated stress [31]. In the context of electric vehicles, battery pack components experience continuous repetitive loading and random vibrations from various sources. These include dynamic inputs such as steering, acceleration, deceleration, and the impact of road irregularities like bumps and cracks. Such dynamic forces can lead to stress concentrations, particularly at critical joints within the battery pack. As a result, a thorough durability assessment of EV battery packs must include all joints, including the often-overlooked battery terminal connections. Therefore, it is crucial to develop and implement a robust methodology for evaluating the durability of these cell connections. A reliable fatigue life prediction method is necessary for optimizing both the design and performance of EV battery packs, ensuring that they meet the demands of real-world operating conditions and enhancing their overall reliability and longevity.

### 2.5.1 Rupp's Model Application

Unfortunately, a fatigue prediction model specifically for Al-Cu laser welded joints has yet to be established in previous studies. As shown in

**Figure 9**, battery terminals are commonly connected using circular weld seams, which closely resemble spot welds in appearance, structure, functionality, and failure modes. Although a fatigue prediction model for circular laser welded joints is still needed, the fatigue life prediction method for spot weld joints developed by Rupp et al. [32] is well-established and has been incorporated into commercial fatigue and durability analysis software, nCode DesignLife [33]. Rupp's model provides several notable advantages, including ease of use, computational efficiency, and the flexibility to handle various loading and boundary conditions. These features make it a valuable tool for fatigue analysis in complex structures. Given the functional and geometric similarities between circular laser welds and spot welds, the applicability of Rupp's model to predicting the fatigue life of circular laser-welded joints is investigated in this study. This exploration is motivated by the model's proven effectiveness in analyzing spot welds, which share similar characteristics with circular laser welds. However, due to inherent differences in bonding mechanisms between circular laser-welded joints and resistance spot weld (RSW) joints, there is a need to evaluate and potentially modify the model to account for these variations.

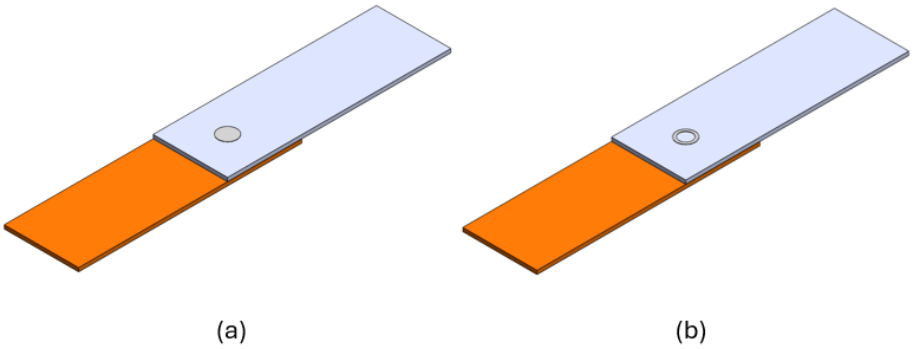



**Figure 9: Schematic illustrating the differences between (a) spot weld and (b) circular laser weld**

In typical battery packs, which consist of numerous laser-welded cell-to-cell connections, it is inefficient to model each joint in a finite element analysis with fine meshes [34]. Instead, Rupp's model utilizes coarse finite element models to minimize computational time while still providing reliable fatigue assessments. Since the stress information from coarse finite element models can be less accurate, Rupp's method employs nodal forces and moments, which are less dependent on mesh density, to calculate structural stress [34]. This approach allows for the estimation of stress states and the conversion of experimental load-life results into stress-life data. By consolidating results from various experiments into a unified chart, the model significantly reduces scatter in stress-life results compared to load-life results, allowing the creation of a master curve for more accurate fatigue life predictions. The adaptation of Rupp's model in nCode further refines stress-life results through statistical optimization of empirical factors.

### 2.5.2 Area Contact Method

The original Rupp's method models each sheet metal components using linear elastic shell elements and each spot weld as a rigid beam element (CBAR element in NASTRAN or B31 element in ABAQUS), as seen in Figure 10. In this approach, the ends of each beam element are kinematically coupled to the corresponding nodes on both sheets. Forces and moments transmitted through these beam elements are used to compute structural stresses at discrete points along the weld perimeter in both the weld nugget and the adjoining sheet metal. These stresses are then employed to predict the fatigue life of the weld using the S-N (stress-life) method [33]. However, this CBAR-based approach has several notable drawbacks. One major issue is that it can lead to structural models with reduced

global stiffness, which may cause inaccuracies in vibrational modes and dynamic behavior. Additionally, the requirement for CBAR elements to remain perpendicular to the sheet surfaces adds complexity to mesh generation. This constraint necessitates nearly congruent meshes on the opposing flanges, which can be challenging to achieve and may further complicate the modeling process.

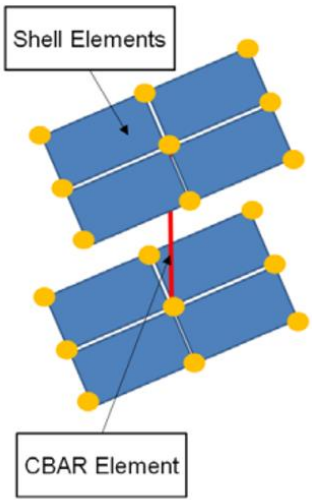



**Figure 10: Schematic representation of the CBAR method for spot weld modeling** [35]

To address these limitations, Heiserer et al. [36] introduced a novel approach known as "Area Contact Methods". This method offers significant advantages over the traditional approach. Notably, it allows for the automatic generation of spot weld joints using commercial meshing tools and congruency between the meshes of opposing flanges is not necessary. This flexibility enables independent meshing of sheet metal components and allows for the easy relocation of spot welds. Furthermore, it is possible to exhibit more realistic global stiffness by fine-tuning the cross-sectional area of the spot weld elements. This feature enhances the accuracy of the simulations and ensures that the models better represent the actual physical behavior of the components, allowing this method to be more versatile in other engineering disciplines such as noise, vibration, and harshness (NVH) analysis.

The Area Contact Method improves load distribution by incorporating a network of rigid elements, which efficiently transfers the load to the surrounding mesh. In this method, the weld nugget is represented by a single hexahedral element (CHEXA in NASTRAN or C3D8 in ABAQUS), which is connected to the nodes of the shell elements using multi-point constraints or equivalent elements (such as RBE3 in NASTRAN or DCOUP3D in ABAQUS). Figure 11 shows a typical implementation of the

ACM model, where each patch consists of four coupling elements, shown as dashed red lines, and each node of the hexahedral element, shown as sold red lines, is connected to four nodes of the surrounding patches. Despite these modifications, the fundamental principles of the Rupp's model remain consistent. Cross-sectional forces and moments are still used to derive stresses, which are then employed in stress-life fatigue calculations.

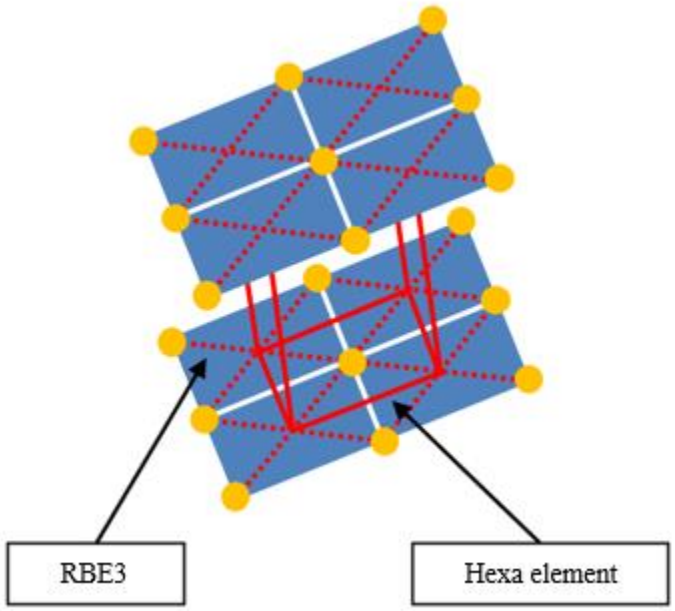



**Figure 11: Schematic representation of the ACM method** [35]

### 2.5.3 Forces and Moment Recovery

To integrate the Area Contact Method with Rupp's model, which uses a single bar element to represent the weld, several modifications are required. Initially, the forces transmitted through the nodes of the hexahedral elements are transformed from global to local coordinates. Then, these forces represented in local coordinates are transferred to the centroids of the top and bottom faces, creating an equivalent "bar element" as seen in Figure 12. During the post-processing stage of finite element analysis, the forces and moments extracted at the ends of this equivalent bar element are then used to determine the structural stresses in the sheets.

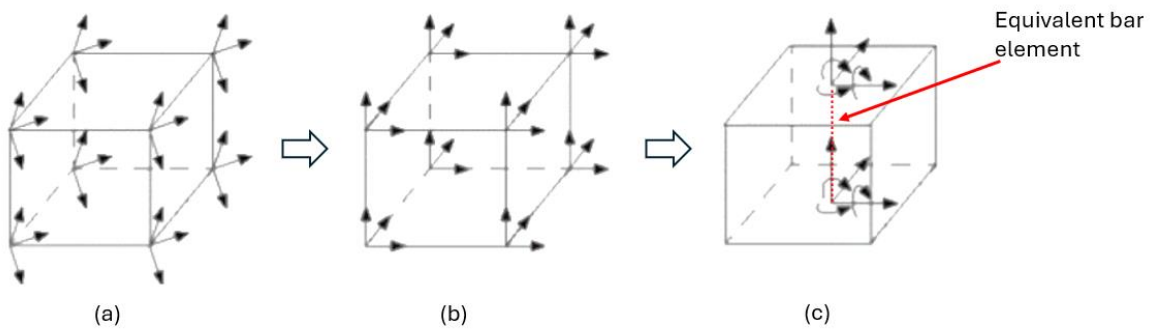



**Figure 12: Transformation of forces from (a) global coordinates (b) local coordinates and then transferred to (c) the centroids of the top and bottom faces** [33]

### 2.5.4 Stress Calculations

The structural stresses in the sheets are the radial stresses that act along the inner surfaces of both sheets around the perimeter of the weld nugget, as illustrated in Figure 13. The calculation of these structural stresses is detailed in equation (1), which accounts for contributions from various forces and moments: shear forces ($F_x$, $F_y$) given in Equations (2) and (3), axial force ($F_z$) given in Equation (4), and bending moments ($M_x$, $M_y$) outlined in Equations (5) and (6). By incorporating these individual contributions into Equation (1), the total structural stress is determined. The sine and cosine functions of these equations allow calculation of stress values at any radial angle ($\theta$) around the weld circumference. In a well-designed structure, most spot welds are not subjected to significant torsional loads under normal operating conditions. Therefore, torsional fatigue is considered negligible, allowing the torsional load (Mz) to be omitted from the stress analysis.

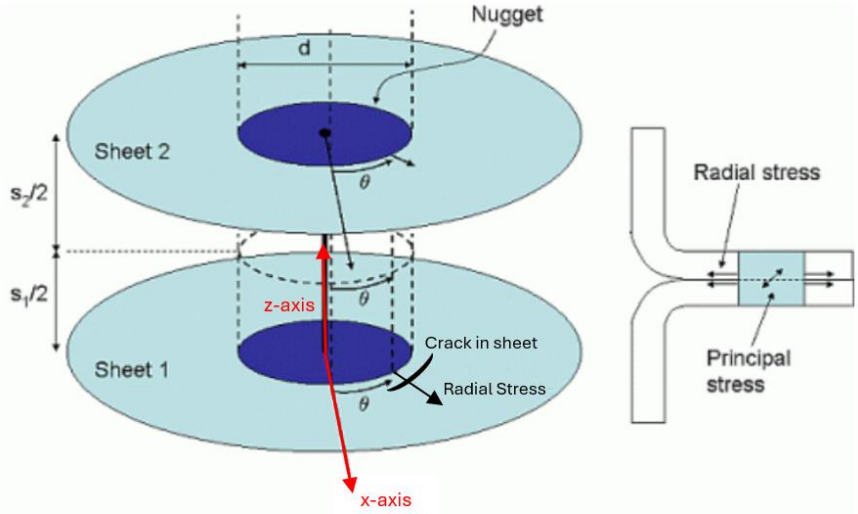



**Figure 13: Simplified schematic of a spot weld, illustrating the radial stresses from the inner surfaces of the two sheets** [33]

$$\sigma_{sheet} = -\sigma_{max}(F_x)cos\theta - \sigma_{max}(F_y)sin\theta + \sigma_{max}(F_z) + \sigma_{max}(M_x)sin\theta - \sigma_{max}(M_y)cos\theta \quad (1)$$

where

$$\sigma_{max}(F_x) = \frac{F_x}{\pi ds} \times SFFXY \times d^{DEFXY} \times s^{TEFXY} \quad (2)$$

$$\sigma_{max}(F_y) = \frac{F_y}{\pi ds} \times SFFXY \times d^{DEFXY} \times s^{TEFXY} \quad (3)$$

$$\sigma_{max}(F_z) = \frac{1.744 \cdot F_z}{s^2} \times SFFZ \times d^{DEFZ} \times s^{TEFZ} \quad if\ F_z > 0\ or\ F_z \leq 0 \quad (4)$$

$$\sigma_{max}(M_x) = \frac{1.872 \cdot M_x}{ds^2} \times SFMXY \times d^{DEMXY} \times s^{TEMXY} \quad (5)$$

$$\sigma_{max}(M_y) = \frac{1.872 \cdot M_y}{ds^2} \times SFMXY \times d^{DEMXY} \times s^{TEMXY} \quad (6)$$

where, $d$ is the weld diameter and $s$ is the sheet thickness.

There are nine empirical factors within these equations. SFFXY, SFFZ, and SFMXY are scale factors used to adjust the contributions of the shear forces, axial forces, and bending moments, respectively, according to different loading geometries. DEFXY, DEFZ, DEMXY, TEFXY, TEFZ, and TEMXY are the factors that account for size effects, such as weld diameter and sheet thickness. The value of nine empirical factors, experimentally determined and incorporated into the commercial fatigue and durability assessment software, nCode DesignLife, for aluminum and steel spot welded joints are summarized in Table 3 and Table 4, respectively.

**Table 3: nCode typical empirical factors for spot welds in steel**

| Component | Factor | Diameter Exponent | Thickness Exponent |
|---|---|---|---|
| $F_x$, $F_y$ | SFFXY = 1.0 | DEFXY = 0.0 | TEFXY = 0.0 |
| $M_x$, $M_y$ | SFMXY = 0.6 | DEMXY = 0.0 | TEMXY = 0.5 |
| $F_z$ | SFFZ = 0.6 | DEFZ = 0.0 | TEFZ = 0.5 |

**Table 4: nCode typical empirical factors for spot welds in aluminum**

| Component | Factor | Diameter Exponent | Thickness Exponent |
|---|---|---|---|
| $F_x$, $F_y$ | SFFXY = 0.4 | DEFXY = 0.5 | TEFXY = -0.25 |
| $M_x$, $M_y$ | SFMXY = 0.4 | DEMXY = 0.5 | TEMXY = -0.25 |
| $F_z$ | SFFZ = 1.0 | DEFZ = 0.0 | TEFZ = 1.0 |

### 2.5.5 Statistical Optimization

The empirical factors in the structural stress equations are highly dependent on the data used. To enhance Rupp's model by improving data collapse when converting load-life to stress-life data, statistical optimization techniques can be employed to refine these empirical factors. In this study, the Generalized Reduced Gradient (GRG) method, introduced in 1977 [37], is utilized for this purpose. The GRG method is a direct approach to nonlinear optimization that simplifies the problem by converting constrained optimization into an unconstrained one. This is achieved by solving equality

constraints for the state (dependent) variables in terms of the design (independent) variables. The resulting unconstrained nonlinear programming problems are then addressed using efficient techniques such as the steepest descent method, conjugate gradient method, and quasi-Newton methods. The nonlinear GRG method implemented in Microsoft Excel's Solver add-in is detailed in [34] and documented in [38].

# Chapter 3
# Laser Weld Characterisation

This chapter presents the initial development and optimization of laser weld process windows to create robust Al-Cu joints. A comprehensive characterisation of these joints, produced under optimal welding conditions, is conducted at both macroscopic and microscopic levels. The analysis aims to investigate the microstructure and mechanical properties of the welds, providing critical insights into their performance and strength.

## 3.1 Laser Welding Process Window and Optimization

### 3.1.1 Experimental Setup

The experimental setup for the Al-Cu laser welding process is shown in Figure 14. This setup consists of an IPG YLS-8000-S4T fiber laser system, operated in continuous mode with a maximum power of 8 kW, a wavelength of 1068 nm, and a Gaussian beam intensity distribution. Notably, shielding gas was not employed during the welding process as a previous study [39] demonstrated that its use has minimal impact on the weld's mechanical properties, affecting primarily the surface appearance rather than the overall performance. The laser system is equipped with a core delivery fiber, available in two diameters,150 μm and 300 μm, resulting in spot sizes of 0.3 mm and 0.6 mm, respectively, with a focal length of 300 mm. In this experimental study, 0.8 mm thick sheets of 110 copper (99.9% Cu) and 1100 aluminum (Al > 99% Al, 0.55-0.95% Si+Fe) were utilized as the base metals. These commercially pure materials are widely used in electric vehicle battery terminal applications due to their excellent electrical conductivity and corrosion resistance.

To prepare the welding samples, the oxide layers on the surfaces of the metals were mechanically removed and wiped with acetone to remove any residual contaminants that might affect the welding quality. Following the recommendations from multiple studies [39], [40], a custom weld fixture was designed to securely clamp the sheets together, ensuring minimal gaps between the aluminum and copper sheets during the welding procedure. To ensure consistency, the welding direction was aligned parallel to the rolling direction of both the aluminum and copper sheets. Additionally, Al-Cu (aluminum on top) configuration was specifically chosen, as opposed to Cu-Al (copper on top) configuration, in order to enhance mechanical properties of the welds and expand the process window as supported by

previous studies [11], [41]. Another issue is the higher reflectivity of copper typically requires it to be on the bottom, whereas lap welding of Cu-Al joints can be achieved with a blue laser in the 400 nm range which is more readily absorbed by copper on top [42].

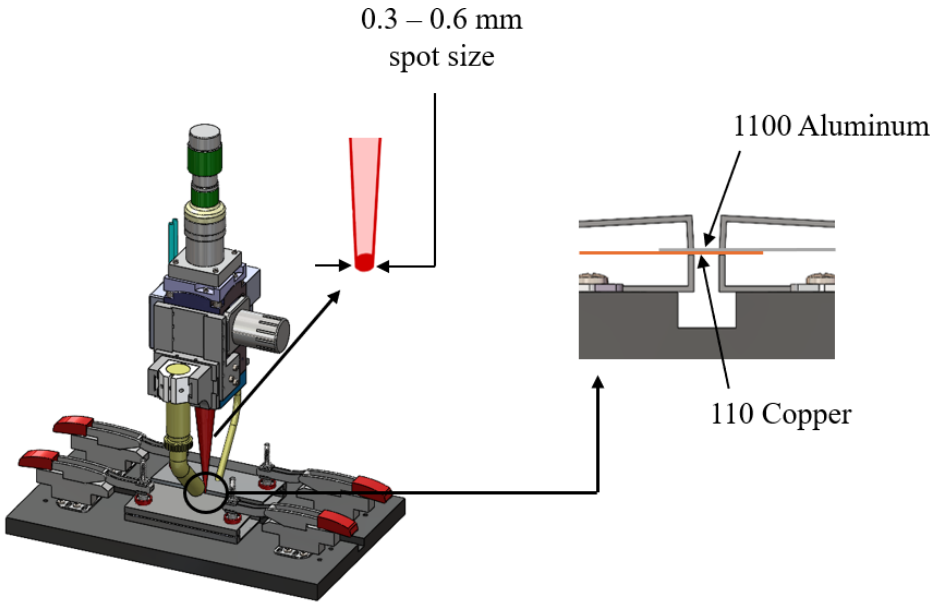



**Figure 14: Laser welding experimental set-up with fixture**

Tensile shear tests were conducted at room temperature to evaluate the mechanical properties of the laser-welded joints and to determine the optimal welding parameters. The samples for these tests were cut into coupons measuring 25.4 mm x 101.6 mm, and arranged in a lap-joint configuration, as shown in Figure 15. The weld, depicted by a blue line, was centrally positioned within the overlap of the aluminum and copper sheets, extending across the entire width. The tensile testing setup is illustrated in Figure 16. These tests were performed using a Tinius-Olsen HK10 tabletop tensile test machine which directly measures load and displacement during the test. For these tests, grips were clamped onto both ends of the copper and aluminum specimens, with each grip clamping a 25.4 mm × 25.4 mm section. The specimens were subjected to a tensile load perpendicular to the welding direction, with a controlled displacement rate of 0.25 mm/min.

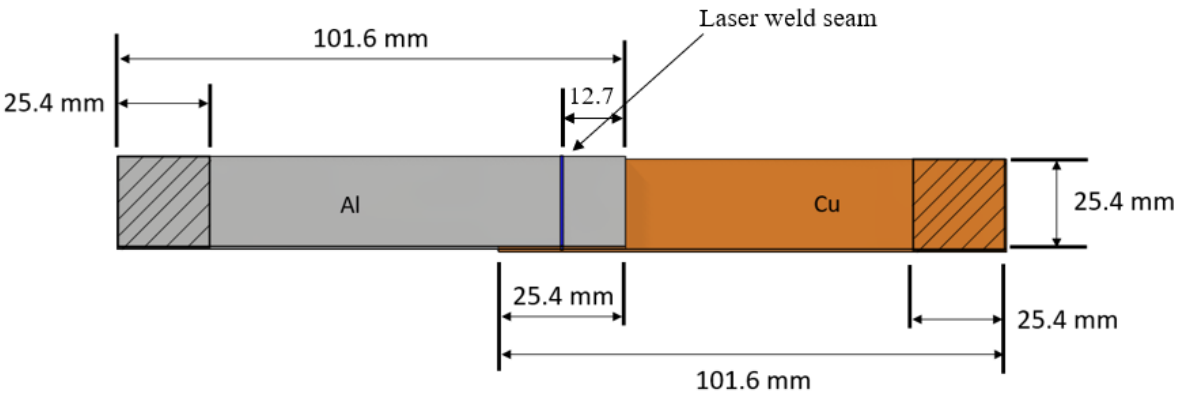



**Figure 15. Lap shear specimen**

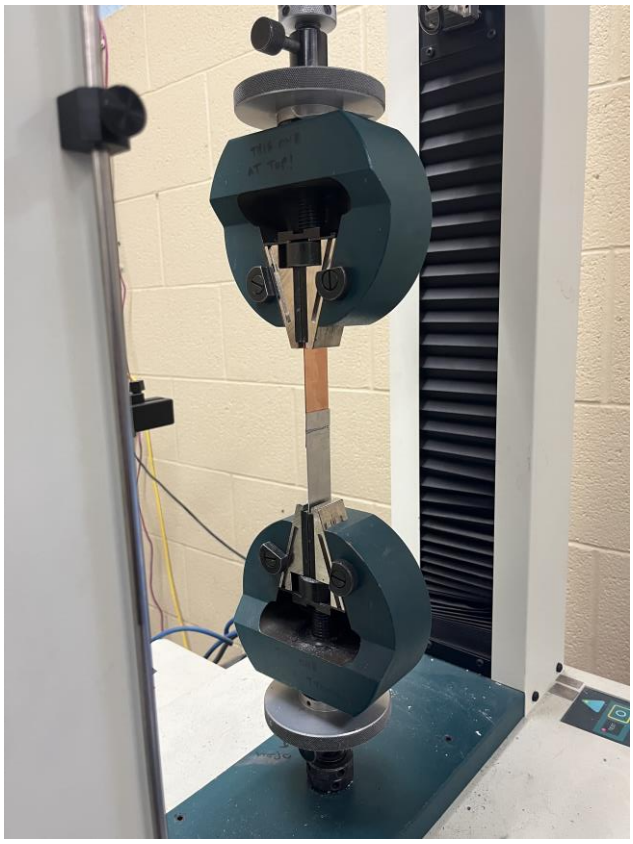


**Figure 16: Tensile testing experimental test setup**

### 3.1.2 Process Window

Due to significant differences in thermo-mechanical characteristics between aluminum and copper as discussed in section 2.1, precise adjustments to the welding parameters are necessary to achieve optimal weld quality. To investigate the effect of laser welding parameters such as laser power and welding speed on the quality and characteristics of the welds, a systematic experimental approach was employed. For this study, both laser welding parameters, welding speed and laser power, were normalized relative to the maximum welding speed and laser power utilized, respectively. Laser welding was conducted at normalized welding speeds of 0.25, 0.5, 0.75, and 1, covering a broad range of welding speeds in industry-level manufacturing. For each welding speed, the normalized laser power was adjusted in incremental steps of approximately 0.03, to precisely control the energy input. This experimental design allowed establishment of a suitable process window to achieve high-quality Al-Cu joints.

As described in Table 5, all welds was evaluated using qualitative measures such as “under-welded”, “good weld” and “over-welded” which are terms commonly used in previous research of dissimilar welding to qualitatively describe conditions of the welds achieved [20], [27], [43]. Welds were classified based on their observed characteristics as follows:

1. “Under-welded”: Welds were identified as “under-welded” when the heat transferred from the laser beam was insufficient to adequately melt the aluminum and achieve proper mixing with the copper. As a result, the welding process demonstrated insufficient joining of the materials, characterised by incomplete penetration or weak bonding. This condition indicates that the welding parameters were set too low, preventing the formation of a reliable joint.
2. “Good weld”: Welds were identified as “good weld” when the aluminum did not fully penetrate the copper sheet, yet still exhibited proper fusion and bonding without excessive mixing or defect formation. These welds displayed a uniform appearance with minimal visible defects in the weld seam and cross-section, indicating that appropriate welding parameters were chosen.
3. “Over-welded”: Welds were categorized as “over-welded” when defect such as humping, perforations, burn-through zones along the bead, or excessive porosity and cracks in the cross-section were observed. These issues typically arise from high heat input, which leads to excessive melting and mixing of the materials. The presence of such defects is an indication that the power density is too high, leading to undesirable outcomes.

To evaluate both the feasibility and quality of the welds, linear welds measuring 10 cm in length were produced for each specific combination of welding speed and laser power, as illustrated in Figure 17. The evaluation process involved a visual inspection of the weld seam on both the aluminum and copper sides, and examination of the weld cross-section.

**Table 5: Weld evaluation terminologies and descriptions**

| | Description | Weld seam | Cross-section |
|---|---|---|---|
| Under-welded | Insufficient heat input |  |  |
| Good weld | Minimal defects<br>No full penetration or excessive mixing |  |  |
| Over-welded | Extreme heat input or abnormal stirring |  |  |

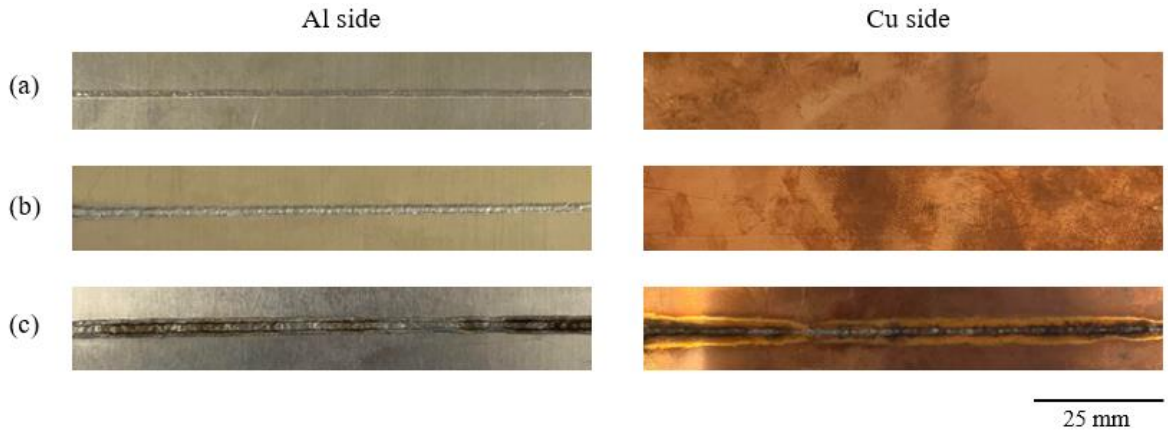



**Figure 17: Example of linear welds: (a) under-welded (b) good weld (c) over-welded**

Through a series of controlled experiments, process windows were developed for laser welding using spot sizes of 0.6 mm and 0.3 mm to join 0.8 mm thick aluminum and copper sheets. These process windows are illustrated in Figure 18 and Figure 19, respectively, where each data point represents a

combination of parameters that were evaluated. Combinations of parameters within the red and blue boundary lines, represented by black data points, resulted in a “good weld” condition. Meanwhile, parameter combinations above the red boundary line, marked by red data points, resulted in “over-welded” joints, and those falling below the blue boundary line, marked by blue data points, resulted in “under-welded” joints.

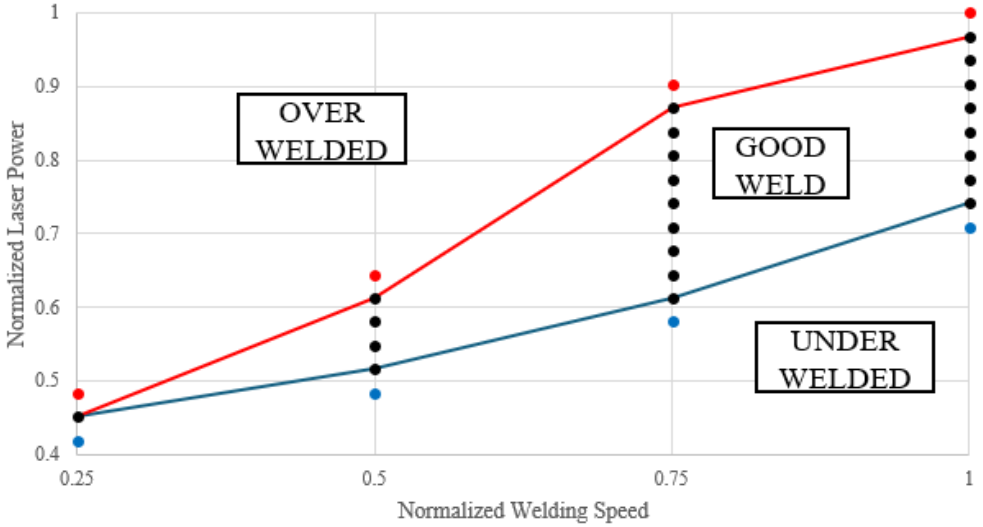



**Figure 18: Laser welding process window for 0.6 mm spot size**




**Figure 19: Laser welding process window for 0.3 mm spot size**

A notable trend observed for both spot sizes was that increasing the welding speed expanded the range of laser power values that could produce "good welds," offering greater flexibility in optimizing the welding conditions. Additionally, as it can be seen in Figure 20, the use of a smaller laser spot size allowed for welding with lower laser power when using the same welding speed, ultimately reducing the total heat input during the process. This reduction in heat input is favorable not only for the structure and properties of weld itself but also for the overall battery pack assembly, which contains heat sensitive chemicals. These findings align with the study by Dimatteo et al., which also reported that employing a smaller spot size contributes to a wider process window, providing better control over penetration depth base material mixing, ultimately improving the quality and consistency of the welds [5].

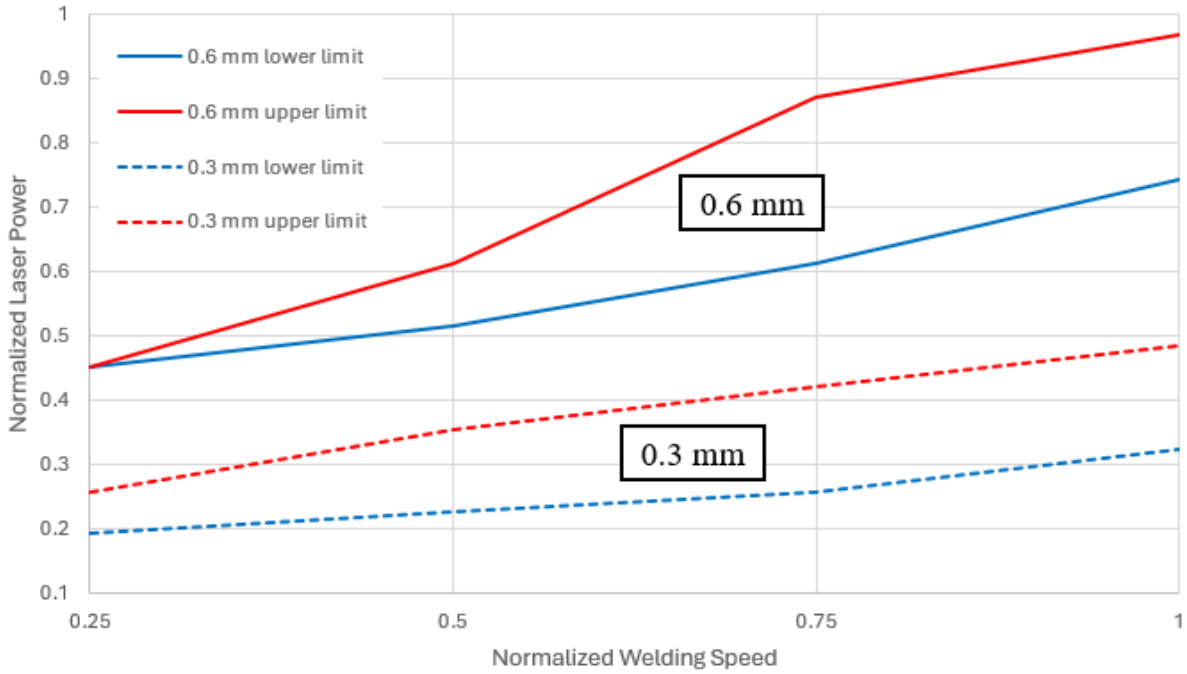



**Figure 20: Laser welding process window for 0.6 mm and 0.3 mm spot sizes combined**

### 3.1.3 Parameter Optimization

Shear tensile tests were conducted to determine the optimal combination of weld parameters that yielded the highest tensile shear strength among all combinations of parameters that were qualified as "good weld". The results of lap shear force, normalized with the lowest lap shear force achieved, are averaged from three to four tests for each parameter set and are presented in Table 6 and Table 7**,** corresponding to spot sizes of 0.6 mm and 0.3 mm, respectively. The data analysis reveals a consistent

trend across both spot sizes: an increase in laser power generally enhances the tensile shear strength for each specified welding speed. For the 0.6 mm spot size, joints created with a normalized welding speed of 0.75 and a normalized laser power of 0.87 achieved a normalized maximum tensile shear load of 15.12. In contrast, for the 0.3 mm spot size, joints produced with a normalized welding speed of 0.5 and a normalized laser power of 0.29 reached a normalized maximum tensile shear load of 17.98. Joints formed with the 0.3 mm spot size generally demonstrated higher maximum shear force with lower standard deviation compared to the joints formed with the 0.6 mm spot size. This behavior can be attributed to several possible factors. A smaller spot size concentrates the heat input more effectively, leading to a more controlled and localized melting process. This results in relatively narrower penetration, along with smaller fusion (FZ) and heat affected zones (HAZ) that can introduce brittleness into the joints. Additionally, these conditions also reduce the formation of intermetallic phases where fracture mainly develops during tensile tests [15], [18]. It is important to note that these tensile shear test results are primarily intended for comparative analysis. Due to the varying levels of penetration associated with each spot size and weld parameters, establishing an equivalent stress is challenging.

**Table 6: Quasi-static tensile test results for 0.6 mm spot size**

| Normalized welding speed | Normalized laser power | Normalized lap shear force | ± SD |
|---|---|---|---|
| 0.25 | 0.45 | 1.00 | 0.50 |
| 0.5 | 0.52 | 1.85 | 0.92 |
| 0.5 | 0.55 | 3.76 | 1.06 |
| 0.5 | 0.58 | 12.76 | 0.65 |
| 0.5 | 0.61 | 14.84 | 1.58 |
| 0.75 | 0.61 | 1.80 | 0.32 |
| 0.75 | 0.65 | 1.86 | 0.95 |
| 0.75 | 0.68 | 3.65 | 1.92 |
| 0.75 | 0.71 | 9.39 | 2.14 |
| 0.75 | 0.74 | 11.34 | 2.20 |
| 0.75 | 0.77 | 11.70 | 1.03 |
| 0.75 | 0.81 | 14.11 | 1.24 |
| 0.75 | 0.84 | 12.90 | 1.72 |
| **0.75** | **0.87** | **15.12** | **1.74** |
| 1 | 0.74 | 1.64 | 1.00 |
| 1 | 0.77 | 4.87 | 0.80 |
| 1 | 0.81 | 8.26 | 1.18 |
| 1 | 0.84 | 9.63 | 1.38 |
| 1 | 0.87 | 10.00 | 2.07 |
| 1 | 0.90 | 10.90 | 2.23 |
| 1 | 0.94 | 13.25 | 0.63 |
| 1 | 0.97 | 12.54 | 1.70 |

**Table 7: Quasi-static tensile test results for 0.3 mm spot size**

| Normalized welding speed | Normalized laser power | Normalized lap shear force | ± SD |
|---|---|---|---|
| 0.25 | 0.19 | 8.67 | 2.78 |
| 0.25 | 0.23 | 10.85 | 0.67 |
| 0.25 | 0.26 | 11.37 | 0.82 |
| 0.5 | 0.23 | 10.52 | 0.46 |
| 0.5 | 0.26 | 13.04 | 1.09 |
| **0.5** | **0.29** | **17.98** | **0.15** |
| 0.5 | 0.32 | 12.58 | 1.13 |
| 0.5 | 0.35 | 14.79 | 0.85 |
| 0.75 | 0.26 | 14.37 | 0.37 |
| 0.75 | 0.29 | 15.12 | 0.71 |
| 0.75 | 0.32 | 13.47 | 1.19 |
| 0.75 | 0.35 | 14.16 | 2.07 |
| 0.75 | 0.39 | 14.22 | 0.41 |
| 0.75 | 0.42 | 15.13 | 0.37 |
| 1 | 0.32 | 11.90 | 0.70 |
| 1 | 0.35 | 12.59 | 1.08 |
| 1 | 0.39 | 13.15 | 1.19 |
| 1 | 0.42 | 15.00 | 1.25 |
| 1 | 0.45 | 14.25 | 0.65 |
| 1 | 0.48 | 14.82 | 0.75 |

## 3.2 Weld Morphology and Microstructure

### 3.2.1 Experimental Setup

To investigate the microstructure of the weld seam, metallurgical cross sections of the joints were prepared. The preparation process involved a series of precise steps including water jet cutting perpendicular to the welding direction, followed by hot mounting in resin. The mounted samples were then ground by using 400#, 800#, 2000# grit SiC paper gradually and polished using diamond and oxide polishing suspensions. To enhance the visibility of microstructural features, the polished sections were etched with Keller's reagent for seven seconds. This etching process attacked the fusion zone, providing contrast and revealing critical details of the microstructure.

Vickers microhardness tests were conducted using a Clemex hardness tester, as seen in Figure 21, to evaluate the impact of the heat affected zone and intermetallic phases on the mechanical properties of the weld. The tests were performed at room temperature across the joint cross-section, applying a 100 g load with a dwell time of 10 seconds and an indentation spacing of 150 μm. The microhardness measurements were carried out along several key regions of the weld. Horizontal indentations were made along the middle of the aluminum side, across the fusion zone, and similarly along the copper side across the weld root. This approach provided a profile of hardness variations across the different weld zones and material phases present in the joint. Additionally, vertical hardness measurements were taken along the centerline of the weld, offering further insights into the gradient of mechanical properties through the thickness of the weld.

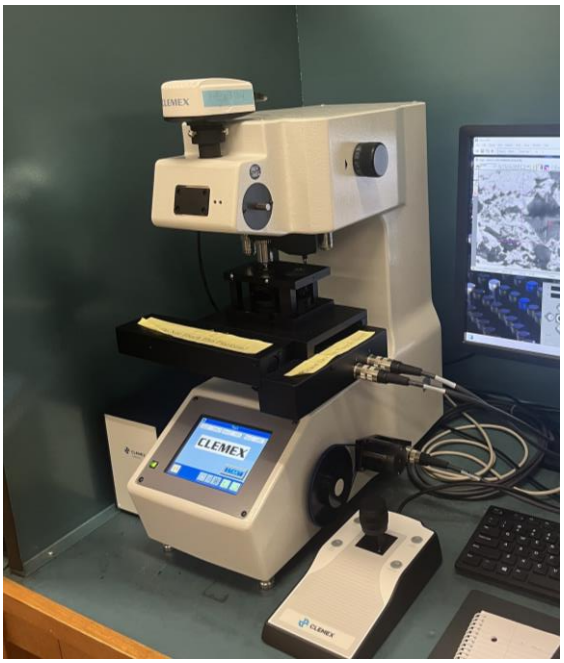



**Figure 21: Microhardness test experimental setup**

The microstructural analysis was conducted using both optical microscopy and field emission scanning electron microscopy. Optical microscopy was performed using a Zeiss Axio Vert.A1 and scanning electron microscopy was performed using a Zeiss Ultra Plus at an accelerating voltage of 20 kV, as seen in parts (a) and (b) of Figure 22, respectively. For elemental composition analysis, Energy Dispersive X-ray Spectrometry (EDS) equipped with the scanning electron microscope was utilized.

EDS was applied to distinct regions of interest identified within the fusion zone near the weld interface to quantify the elemental distribution across the weld and predict the phases using the phase diagram. Furthermore, the predicted intermetallic phases within the weld were verified through X-Ray Diffractometry (XRD) measurements using Bruker D8 Discover, as seen in Figure 22 part (c). Correlating the hardness data with the microstructural analysis allowed to identify different intermetallic phases and assess their influence on the mechanical properties of the weld.

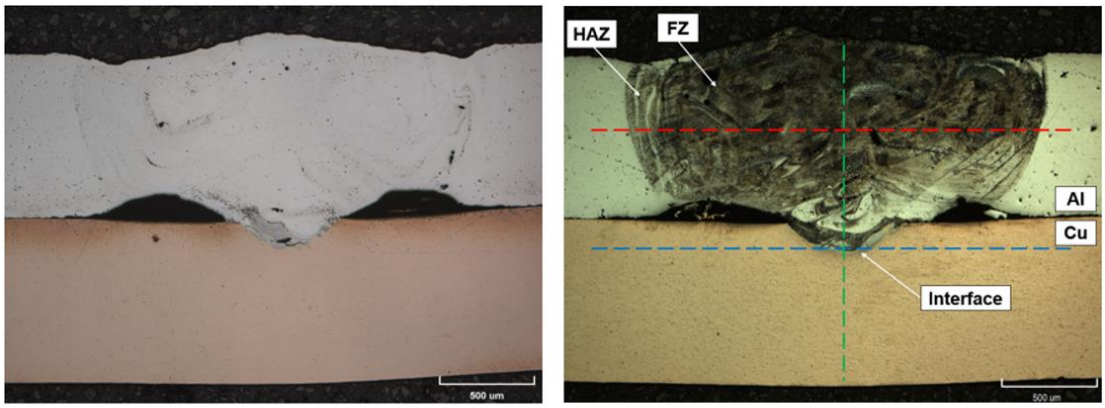



**Figure 22: Setup of (a) optical microscope (b) scanning electron microscope (c) X-ray diffractometers**

### 3.2.2 Weld Cross Section Micrographs and Microhardness

The microhardness values have been normalized relative to the lowest hardness value measured at the aluminum base metal. The optical micrographs in Figure 23 part (a) provides a view of the cross-section of the laser weld produced using the optimal weld parameters (normalized laser power of 0.29 and welding speed of 0.5 using 0.3 mm spot size) previously found in section 3.1.3. Post-etching, the micrograph clearly revealed several distinct regions, including the heat-affected zone, the fusion zone, and the extent of weld penetration, as seen in Figure 23 part (b). Parts (a), (b), and (c) of Figure 24 displays microhardness measurements conducted along the designated red, blue, and green lines of Figure 23 part (b), respectively. An examination of the horizontal microhardness profiles, depicted in parts (a) and (b) of Figure 24, revealed that the hardness values outside of the HAZ and FZ remain relatively stable, closely corresponding to the expected hardness of the base metals. Notably, on the aluminum side, there is a gradual increase in hardness as the measurement progressed toward the HAZ and FZ, indicating a localized strengthening effect due to thermal influences during melting and

resolidifying. Further insights are provided by the microhardness profiles in parts (b) and (c) of Figure 24, where the hardness values remained relatively consistent and as expected along the length of the measurements, except at the weld interface. At this point, there is a significant increase in the normalized micro hardness value, reaching as high as 16.9. According to [3], such a substantial increase in hardness is a strong indicator of the presence of a brittle and hard intermetallic phase within this region.




(a) (b)

**Figure 23. Micrographs of weld seam cross-sections for a joint produced with a normalized laser power of 0.29, a welding speed of 0.5, and a laser spot size of 0.3 mm: (a) unetched sample (b) etched sample, highlighting location microhardness measurements**

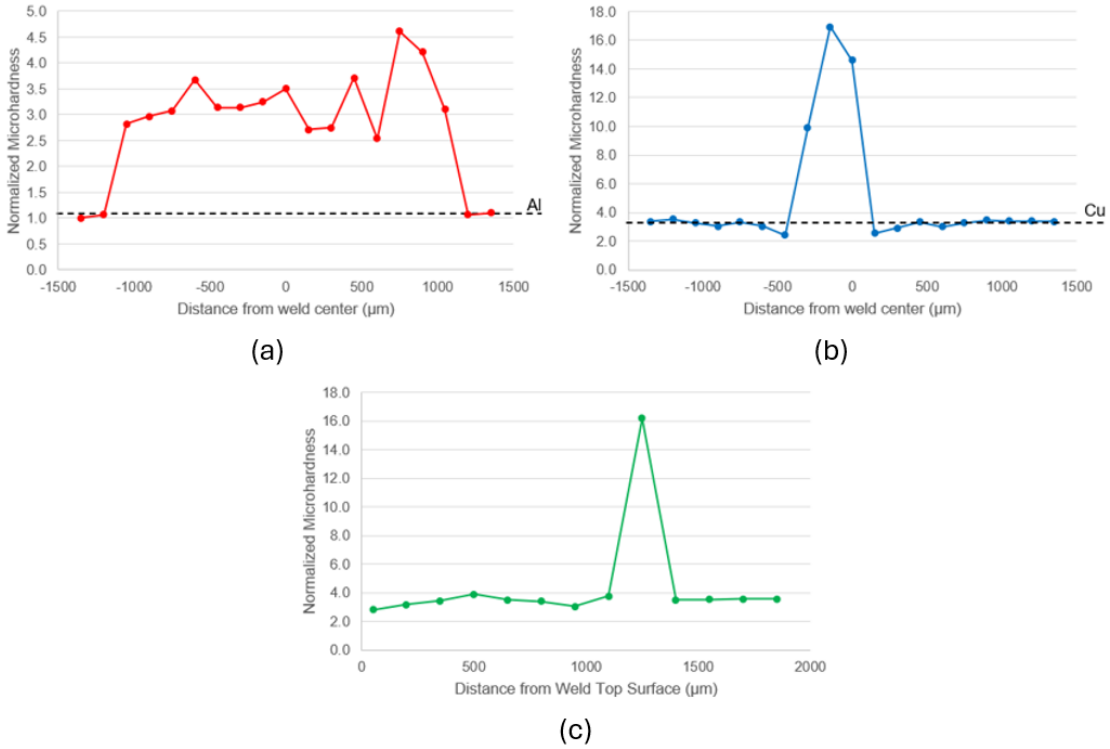



**Figure 24. Microhardness measurements conducted on (a) red line (b) blue line (c) green line depicted on Figure 23**

### 3.2.3 SEM and XRD Analysis

To confirm the presence of intermetallic phases as predicted in section 3.2.2, SEM coupled with EDS analysis was utilized. Figure 25 part (a) presents an SEM image of the entire weld cross-section created using optimal parameters, while part (b) shows a magnified view of the area highlighted by the red box shown in part (a). EDS analysis was conducted at four distinct locations, selected based on image contrast and microstructural variations observed in Figure 25 part (b). The results are summarized in Table 8.

- Selected Area 1: Located farthest from the weld interface, the analysis revealed a composition of 100 wt.% Al. In this region, very fine dendritic structures typical of solidified aluminum were observed
- Selected Area 2: Closer to the weld interface, this area showed composition of 68.0 wt.% Al and 32.0 wt.% Cu. According to the phase diagram, such composition corresponds to the Al +

$Al_2Cu$ hypo-eutectic phase. Figure 26 part (b) shows the presence of both regular and irregular $Al+Al_2Cu$ lamellar structure with Al precipitates in this region.

- Selected Area 3: The analysis identified 43.3 wt.% Al and 56.6 wt.% Cu, which according to the phase diagram suggests a pure intermetallic phase of $Al_2Cu$. This suggests a transition or interface zone where significant diffusion between aluminum and copper occurred. Due to the brittle nature of intermetallic phases, microcracks are visible in this $Al_2Cu$ phase, as shown in Figure 26 part (a). The uniform $Al_2Cu$ phase is shown clearly in Figure 26 part (b).
- Selected Area 4: Located in the copper base metal, the EDS analysis detected 100 wt.% Cu.

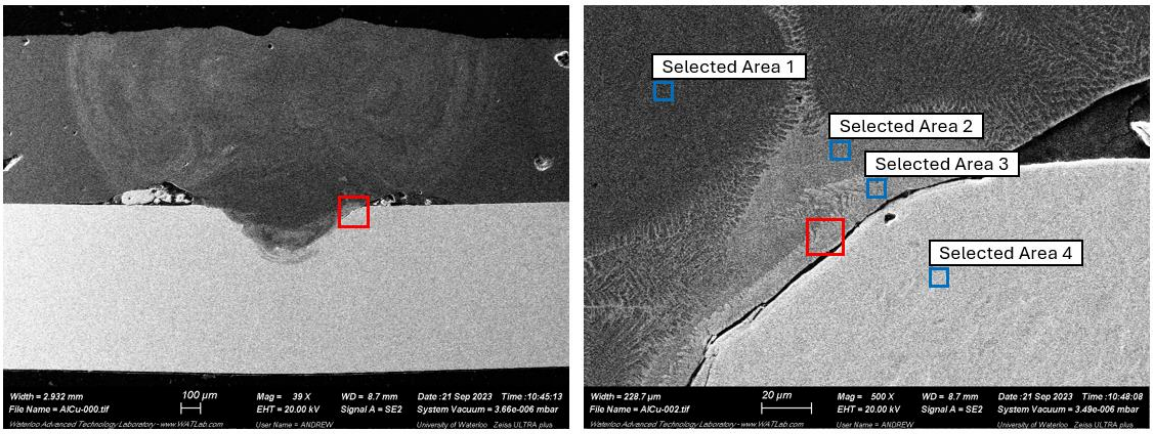



**Figure 25: SEM images of (a) interface of the weld (b) magnified view of the area highlighted by the red box in part (a) showing selected areas for EDS analysis**

**Table 8. EDS analysis of selected areas 1-4 from Figure 25 part (b)**

| Selected Area | wt.% Cu | wt.% Al | Phase |
|---|---|---|---|
| 1 | 0.0 | 100.0 | Al |
| 2 | 32.0 | 68.0 | Al + θ-$Al_2Cu$ |
| 3 | 56.6 | 43.4 | θ-$Al_2Cu$ |
| 4 | 100.0 | 0.0 | Cu |

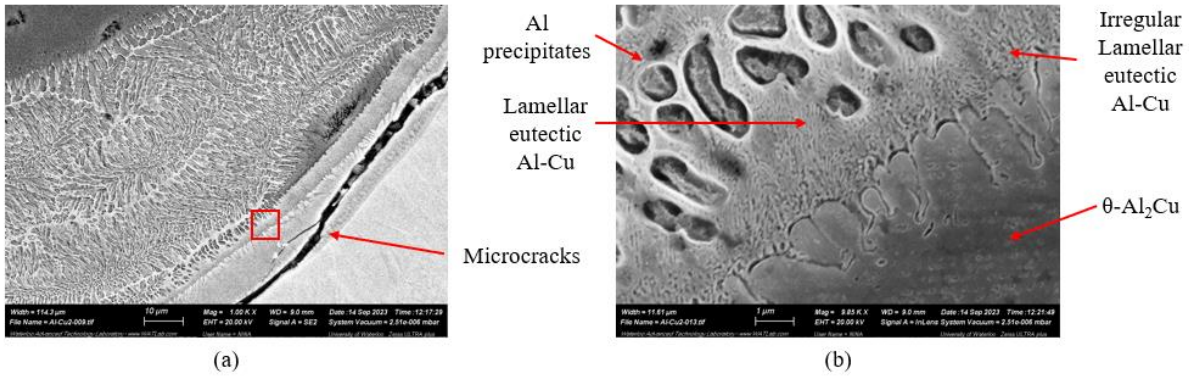



**Figure 26: SEM images of a (a) magnified view of the area highlighted by the red box in part (b) of Figure 25 (b) magnified view of the area highlighted by the red box in part (a)**

To further validate the presence of intermetallic phases, identified through SEM and EDS analysis, XRD analysis was conducted. The x-ray beam, collimated to a diameter of 0.3 mm, was focused on the weld interface near the weld root to target the critical regions where phase transformations were expected. The results are presented in Figure 27. The XRD measurements confirmed that $Al_2Cu$ was the sole intermetallic phase present, agreeing with the findings obtained from the EDS analysis. This validation through XRD strengthens the reliability of the microstructural characterisation and provides a confirmation of the phase composition at the weld interface. The results obtained from this microstructural analysis closely resemble the findings of Yan et al., who also observed the formation of $Al_2Cu$ as the predominant intermetallic phase in Al-Cu laser welded joints [18].

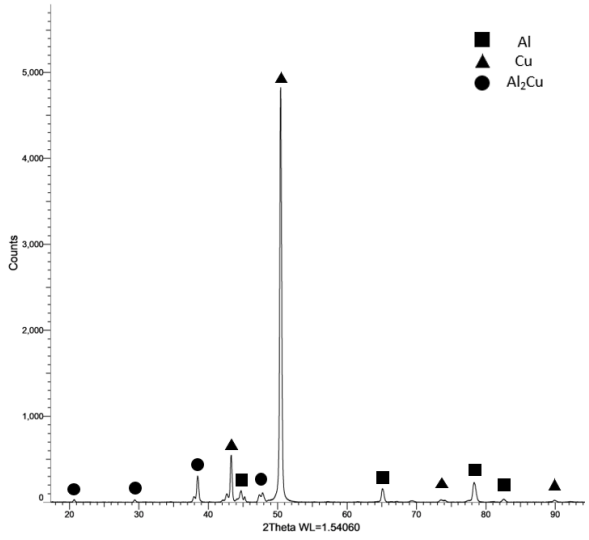



**Figure 27. XRD measurements at weld interface**

# Chapter 4
# Quasi-Static and Fatigue Characterisation

This chapter documents the quasi-static and fatigue experimental results of Al-Cu laser welded joints. Cross-tension coupons were prepared using the optimized parameters found in section 3.1.3 and they have been tested in different loading orientations. The data generated from the experimental results will be used to calculate structural stress.

## 4.1 Experimental Setup

In this study, cross-tension coupons were utilized to evaluate the quasi-static and fatigue behavior of Al-Cu welds due to their capability to demonstrate the complex stress states that these dissimilar metal joints are likely to encounter in practical applications. In the cross-tension configuration, two overlapping flat sheets are joined at their centers, with one sheet rotated 90 degrees in-plane relative to the other. Each sheet, made from 0.8 mm thick 1100 aluminum and 110 copper, was machined into the dimensions shown in Figure 28. For the welding process, a custom fixture was designed to minimize the gap between the sheets, and accurately align and weld the sheets in the cross-tension configuration. A detailed illustration of the welding process using the fixture is shown in Figure 29.

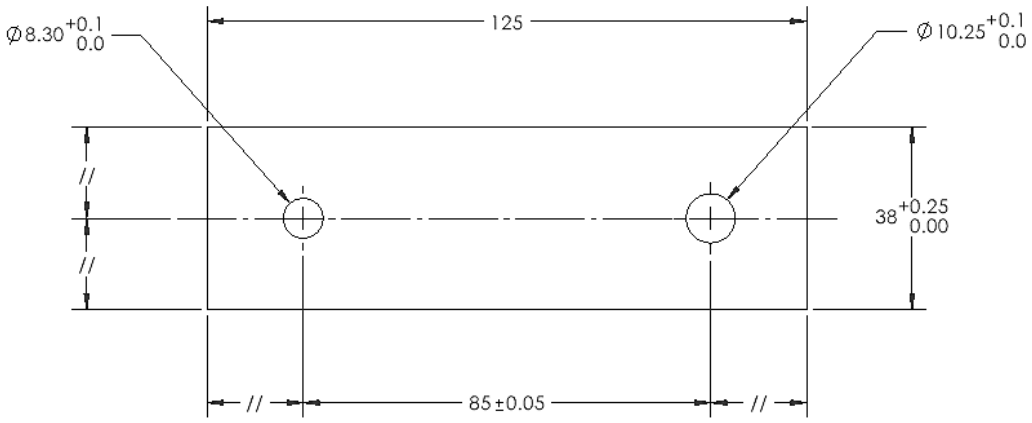



**Figure 28: Sheet dimensions (in mm) for cross-tension specimen sheet metal joint testing**

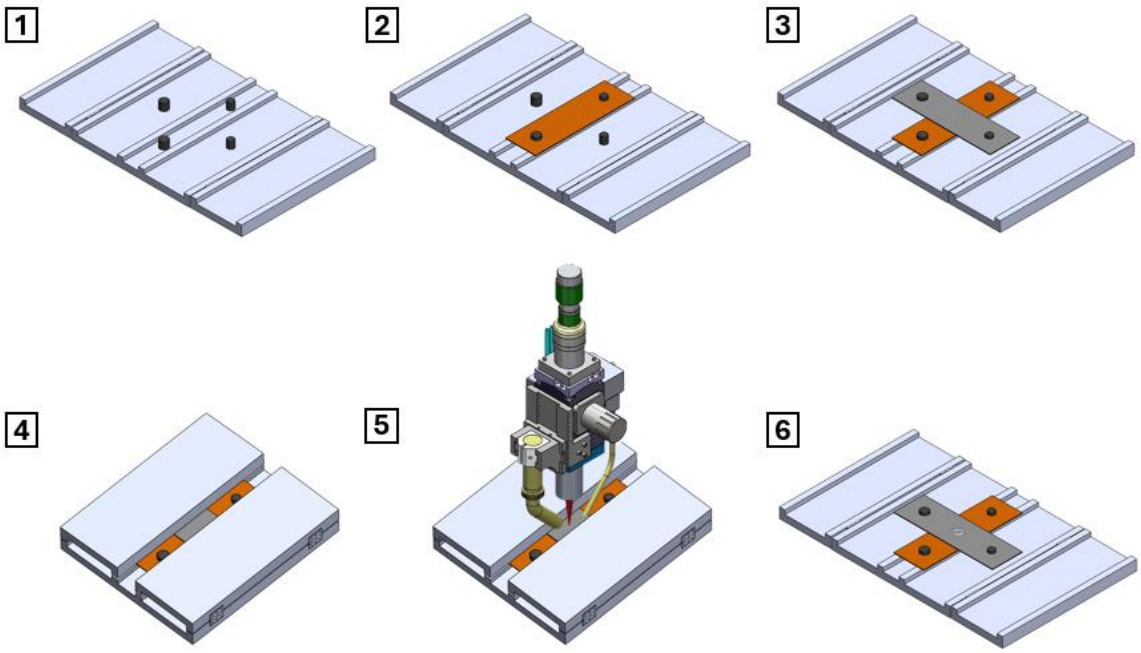



**Figure 29: Welding process showing fixture setup, material placement, clamping, welding operation, and final welded assembly**

Given the widespread use of circular weld seams in battery cell connections due to various advantages, a circular weld seam was specifically selected for this study to align with common industry practices. In specimen-level experiments, a circular weld is particularly beneficial to accurately evaluate the mechanical properties of the joints as it provides more uniform stress distribution across the weld area, reducing the likelihood of stress concentration at specific points under different loading orientations. Unlike linear welds, which tend to be stronger in the direction parallel to the weld but weaker perpendicular to it, the symmetrical nature of a circular weld seam ensures consistent joint behavior regardless of the direction of the applied force. Additionally, the circular weld minimizes edge effects, which are more pronounced in linear welds. This is particularly important in cross tension testing, where the objective is to assess the overall strength and integrity of the weld rather than identifying localized weaknesses. An image of an Al-Cu cross-tension coupon is depicted in Figure 30. Given the constraints of the experimental setup, the diameter of the circular weld used in this study was 8 mm.

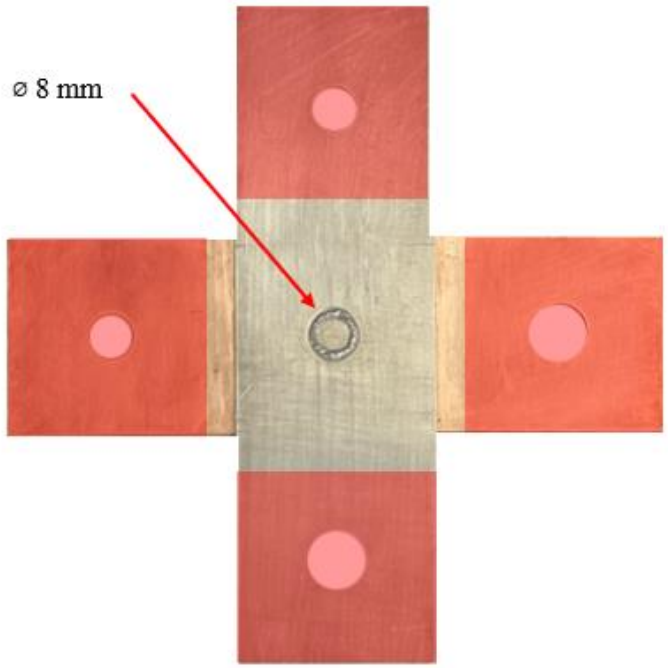



**Figure 30: Al-Cu laser welded cross-tension coupon where red regions represent test fixture clamped areas**

The testing of cross-tension coupons in various loading orientations requires the use of a custom test fixture. For this study, a specialized test fixture, designed at the University of Waterloo, shown in Figure 31, was employed. This fixture allows for both quasistatic and fatigue testing of cross-tension sheet metal joints at loading orientations of 0°, 22.5°, 45°, 67.5°, and 90°, as illustrated in Figure 32, by simply adjusting the position of the grips. For instance, when the grips are positioned as shown in Figure 31, the cross-tension specimen is subjected to a $90^{o}$ loading orientation, where the weld's cross-sectional area, in-plane with the contact interface of the two sheets, experiences pure shear stress. In contrast, at a $0^{o}$ loading orientation, the same area is subjected to pure tension. At a $45^{o}$ loading orientation, or any other intermediate angle between $0^{o}$ and $90^{o}$, the same cross-sectional area undergoes a combined stress state, experiencing both shear and tensile forces. The grips securely hold all four ends of the specimen, which measures 38 × 38 mm, as indicated by the red regions in Figure 30. Once a test specimen is fixed to the testing apparatus, the load frame applies a designated load based on the testing conditions. For quasistatic testing, this is done through a user-specified displacement rate, while fatigue testing involves the application of cyclic loads determined by parameters such as load level, load ratio, and frequency.

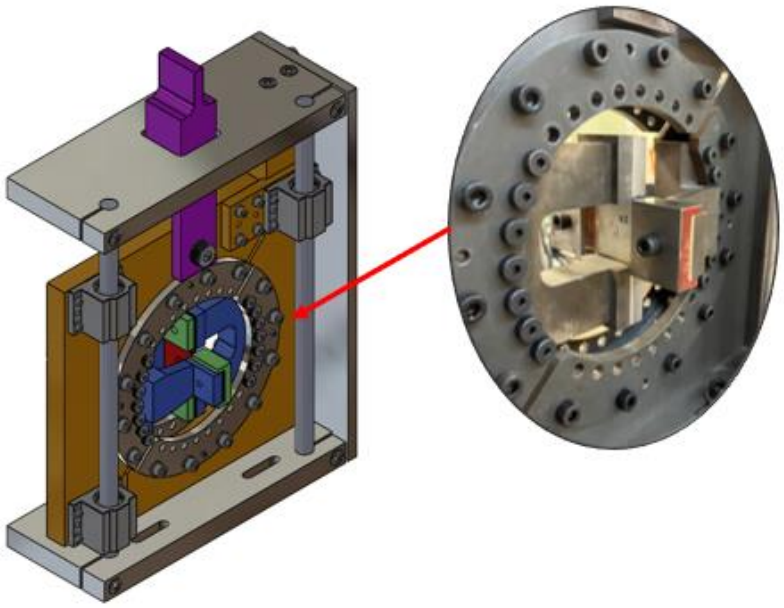


**Figure 31: Cross-tension test fixture in 90º (shear) loading orientation**

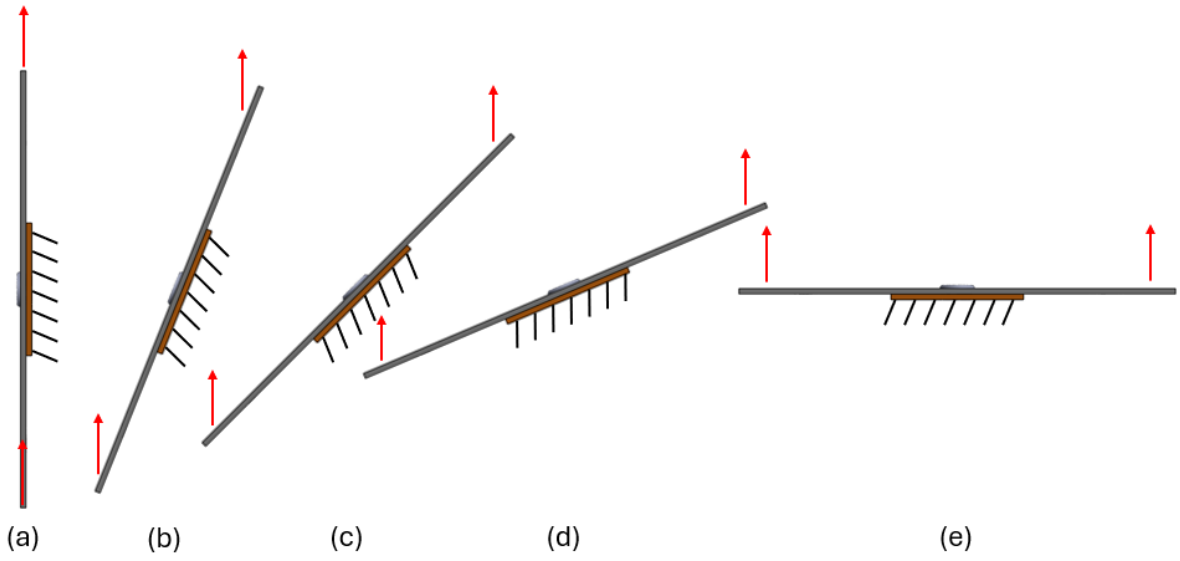



**Figure 32: Examples of cross-tension configurations for laser-welded Al-Cu joints with load applied to aluminum sheet ends and copper ends fixed: (a) 90$^0$ - pure shear (b) 67.5º - combined (c) 45º - combined (d) 22.5º - combined (c) 0º - pure tension**

To investigate the initiation and propagation of cracks during fatigue testing, a series of interrupted tests were conducted. In these experiments, cyclic loading was paused at intervals of 40%, 50%, 60%, 70%, and 80% of the expected fatigue life for detailed examination of the specimen at different stages of fracture progression. Following each interrupted test, the cross-section of the specimen along the loading direction was carefully prepared and analyzed to observe the progression of crack development and assess how fatigue damage progressed over time. For fracture surface analysis, a scanning electron microscopy was performed using a Zeiss Ultra Plus, operating at an accelerating voltage of 20 kV. The high magnification micrographs allowed for a further analysis of the crack morphology and provided insights into the mechanism of crack initiation and growth.

## 4.2 Quasi-Static Behavior

### 4.2.1 Quasi-Static Test Procedure

An Instron 8872 uniaxial fatigue testing system, featuring a 25kN load capacity, was used with the cross-tension fixture to conduct the specimen testing, as shown in Figure 33. For this study, four quasistatic tests were performed for each 90° and 67.5° loading orientations to observe the quasistatic behavior and establish reference load levels for fatigue testing. The remaining specimens were used for fatigue testing. The load frame was operated in displacement control mode, which allowed precise regulation of the displacement rate, set at 0.5 mm/min. Each quasistatic test was carried out until the complete separation of the joints was achieved.

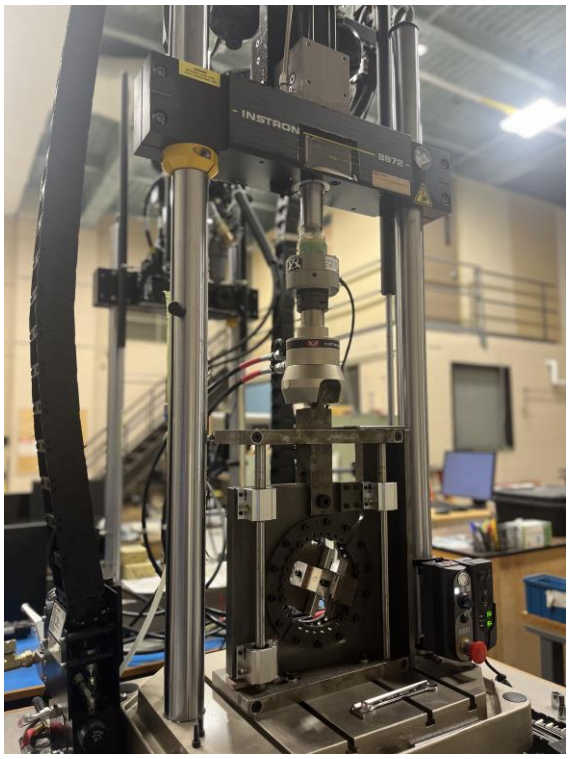



**Figure 33: Instron 8872 with cross-tension fixture**

### 4.2.2 Quasi-Static Experimental Results

The results for the quasi-static tests at a 90$^{o}$ loading orientation are shown in Figure 34, with both load and displacement values normalized to their respective maximum values. The load-displacement curves for all specimens exhibit a similar overall shape, indicating consistent mechanical behavior across the tests. Furthermore, the peak load and displacement values show minimal variation, suggesting uniform weld quality among the specimens. A notable observation was that the specimens with relatively higher peak load (tests 2 and 3) exhibited lower displacement, and the specimens with lower peak load (tests 1 and 4) exhibited higher displacement. Each curve demonstrated a smooth, gradual increase in load as displacement increased, signifying that the welds' load bearing capacity improved progressively with applied displacement. However, all specimens ultimately failed with a sudden drop in load, indicative of brittle failure. These findings suggest that the welds were of uniform quality, and the specimens exhibited repeatable mechanical properties under quasi-static loading conditions.

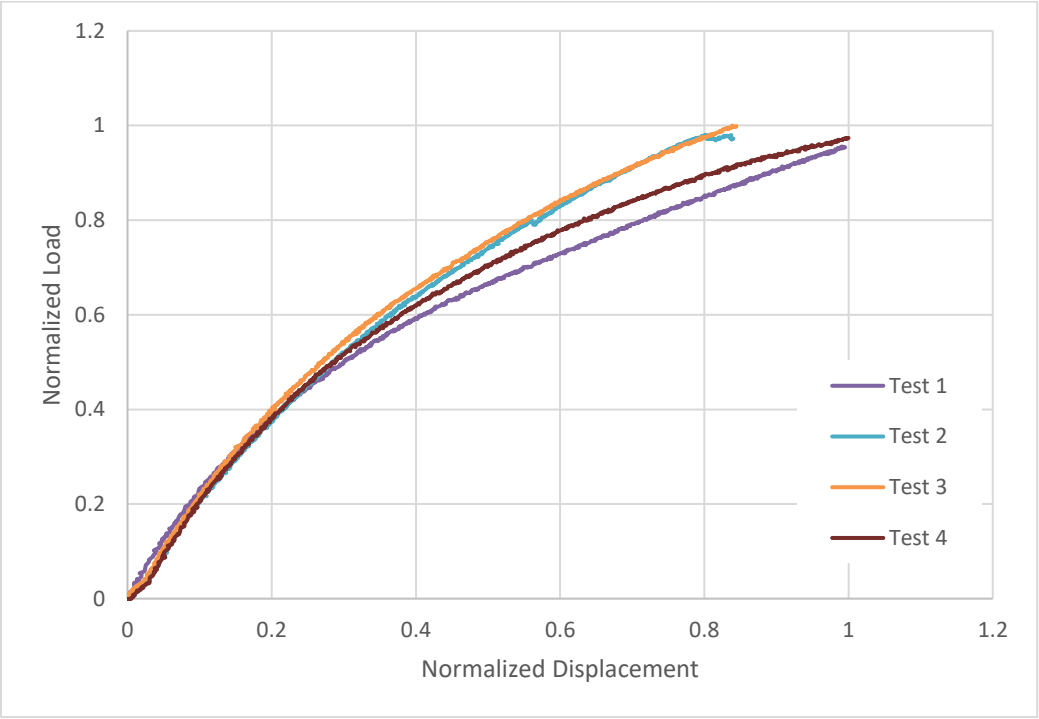



**Figure 34: Quasi-static test results for 90º loading orientation**

The results for the quasi-static tests at a 67.5º loading orientation are shown in Figure 35, with both load and displacement values normalized to the same values as the 90º loading orientation. The consistency across tests is evident, as the specimens exhibit similar load-displacement. While the peak load values for both the 67.5º and 90º orientations remain similar, the peak displacement for the 90º loading orientation was, on average, approximately 13% higher. Similar to the tests in 90º loading orientation, the specimens in the 67.5º orientation experienced a sudden drop in load at failure, indicating a brittle fracture mechanism. In the early stages of testing, up to approximately 0.25 normalized displacement, the load-displacement curves show some irregular and inconsistent behaviors. This irregularity can be attributed to several factors. At this initial stage, the 67.5º loading orientation introduces a combination of shear and tensile stresses, making deformations in the thin base metals more likely to occur before significant deformation in the weld metal. Additionally, the thin sheets used for the cross-tension coupons may present compliance issues, as their higher compliance may affect the accuracy of measurements taken with the load cell used in this study. However, as displacement progresses beyond the initial 0.25 normalized value, the irregularities in the load-displacement curves stabilize, transitioning into a more consistent and predictable trend.

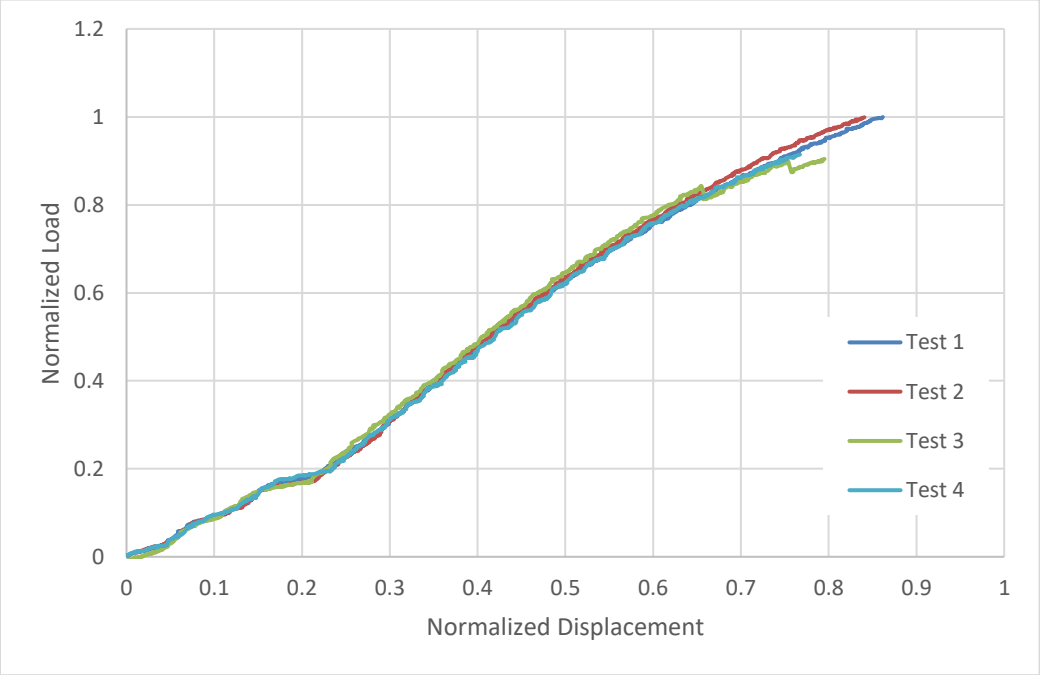



**Figure 35: Quasi-static test results for 67.5º loading orientation**

## 4.3 Fatigue Behavior

### 4.3.1 Fatigue Test Procedure

Cross-tension fatigue tests were performed using the Instron 8872 uniaxial fatigue testing system, the same equipment used for quasistatic testing, with specimens oriented at 90° and 67.5°. These fatigue tests were conducted under controlled loading conditions, with frequency levels adjusted to correspond to the applied load levels. A load ratio of 0.1 was maintained to prevent buckling under compressive loads, ensuring that the fatigue behavior of the welds was accurately captured without introducing additional failure modes. Based on the quasistatic test results, load levels were selected to cover the entire range from low cycle fatigue to runout life of 2,000,000 cycles. Each test was continued until complete separation of the welded joints occurred.

### 4.3.2 Fatigue Experimental Results

The fatigue test matrix and corresponding load-life curve for the 90º loading orientation are presented in Table 9 and Figure 36, respectively. A total of 28 tests were conducted across 9 different load levels, with 2 to 5 replicates at each level, ensuring the reliability and consistency of the experimental results.

The results follow typical fatigue behavior with minimal scatter, where the number of cycles to failure increases as the applied load decreases. Low cycle fatigue was observed at 12,134 and 9,650 cycles for tests conducted at 85% of the peak quasistatic load. In contrast, runout, or the absence of failure, was achieved at 50% of the peak quasistatic load.

**Table 9: Test matrix for fatigue tests in 90º loading orientation with load levels determined from maximum load of quasistatic results and r-ratio = 0.1**

| Max. Load | Min. Load | Amp | Freq. (Hz) | Number of cycles to failure | | | | |
|---|---|---|---|---|---|---|---|---|
| | | | | Test 1 | Test 2 | Test 3 | Test 4 | Test 5 |
| 0.50 | 0.050 | 0.225 | 10 | 2,000,000 | 1,386,191 | 2,000,000 | | |
| 0.53 | 0.053 | 0.248 | 11 | 1,833,270 | 1,098,692 | 556,744 | | |
| 0.57 | 0.057 | 0.266 | 12 | 428,586 | 272,779 | 402,921 | 599,663 | |
| 0.60 | 0.060 | 0.270 | 15 | 413,782 | 337,092 | 395,429 | 482,517 | |
| 0.65 | 0.065 | 0.292 | 15 | 168,293 | 200,937 | 232,675 | | |
| 0.71 | 0.071 | 0.321 | 15 | 157,917 | 147,756 | 135,427 | 49,780 | 72,841 |
| 0.73 | 0.073 | 0.338 | 15 | 31,891 | 58,892 | | | |
| 0.78 | 0.078 | 0.351 | 15 | 42,335 | 43,526 | | | |
| 0.85 | 0.085 | 0.382 | 15 | 12,134 | 9,650 | | | |

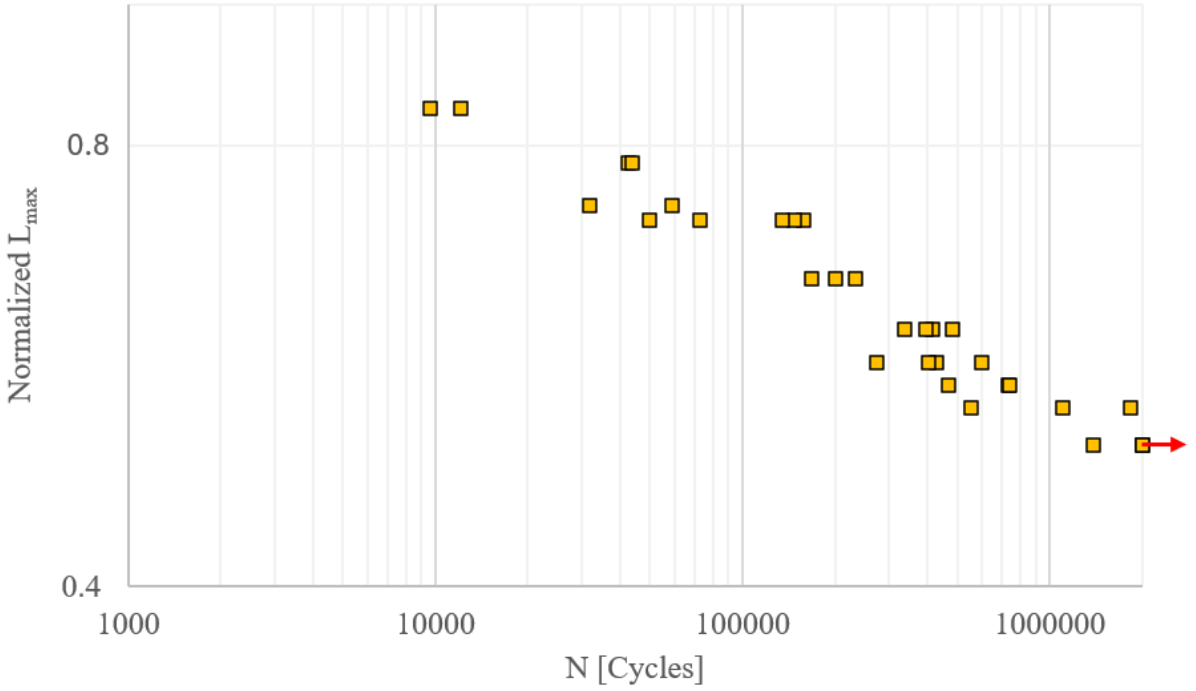



**Figure 36: Load-life curve for 90º loading orientation with arrow indicating runout data**

Each test conducted across all load levels exhibited a consistent failure mode. Specifically, these failures closely resembled one of the common failure modes associated with spot welds: eyebrow failure, where the crack initiates between the two sheets and expands along with the thickness until it fails [44]. An example of this failure mode is shown in Figure 37.

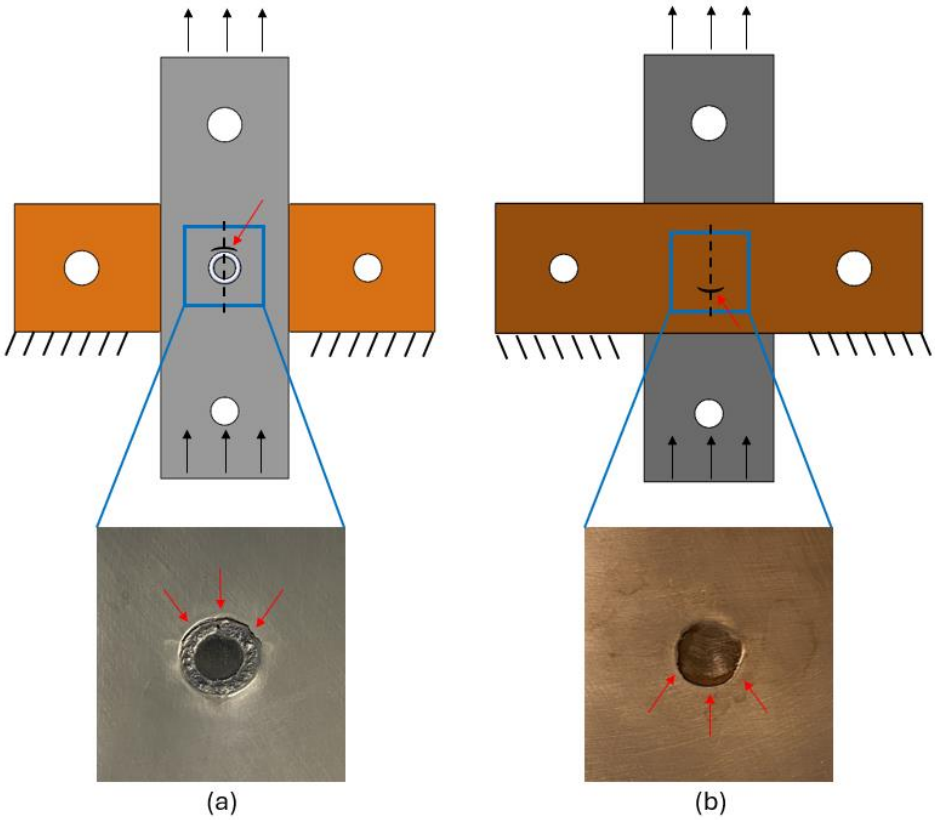



**Figure 37: "Eyebrow" failure mode observed in this study (black arrows showing direction of displacement of the aluminum sheet): cracks observed (red arrows showing location of cracks) on (a) aluminum side (b) copper side**

Since the crack initiates at the interface between the two sheets, real-time monitoring of crack initiation and propagation during testing was not feasible. To gain a deeper understanding of the failure mechanisms, a series of interrupted tests were conducted. Figure 38 provides schematic representations and micrographs of the weld cross-sections from these interrupted tests, with each row corresponding to different stages of the specimens' fatigue life. It was observed that no cracks initiated until approximately 50% of the expected life had elapsed. At this stage, a crack was detected at the bottom of the fusion zone (weld root) on the copper side, highlighted by a red arrow, while no corresponding cracks were found on the aluminum side. The initiation of cracking on the copper side can be attributed to several potential factors. As discussed in section 3.2.3, the presence of intermetallic compounds at the weld root is a likely contributor. These compounds often exhibit brittle behavior, making the material more susceptible to crack initiation under cyclic loading conditions. Additionally, the

geometric characteristics of the weld root significantly influence the crack behavior. Specifically, the sharp edges at the weld root can introduce a notch effect, resulting in a localized stress concentration zone that facilitates crack initiation. At 60% of the expected life, the crack on the copper side propagated downwards through the thickness of the copper, while crack initiation was observed in the heat-affected zone of the aluminum side at the interface between the aluminum and copper sheets. By 70% of the expected life, the crack on the copper side had fully propagated, and the crack on the aluminum side began to propagate upward through the thickness of the aluminum. Finally, at 80% of the expected life, the crack on the aluminum side had also fully propagated.

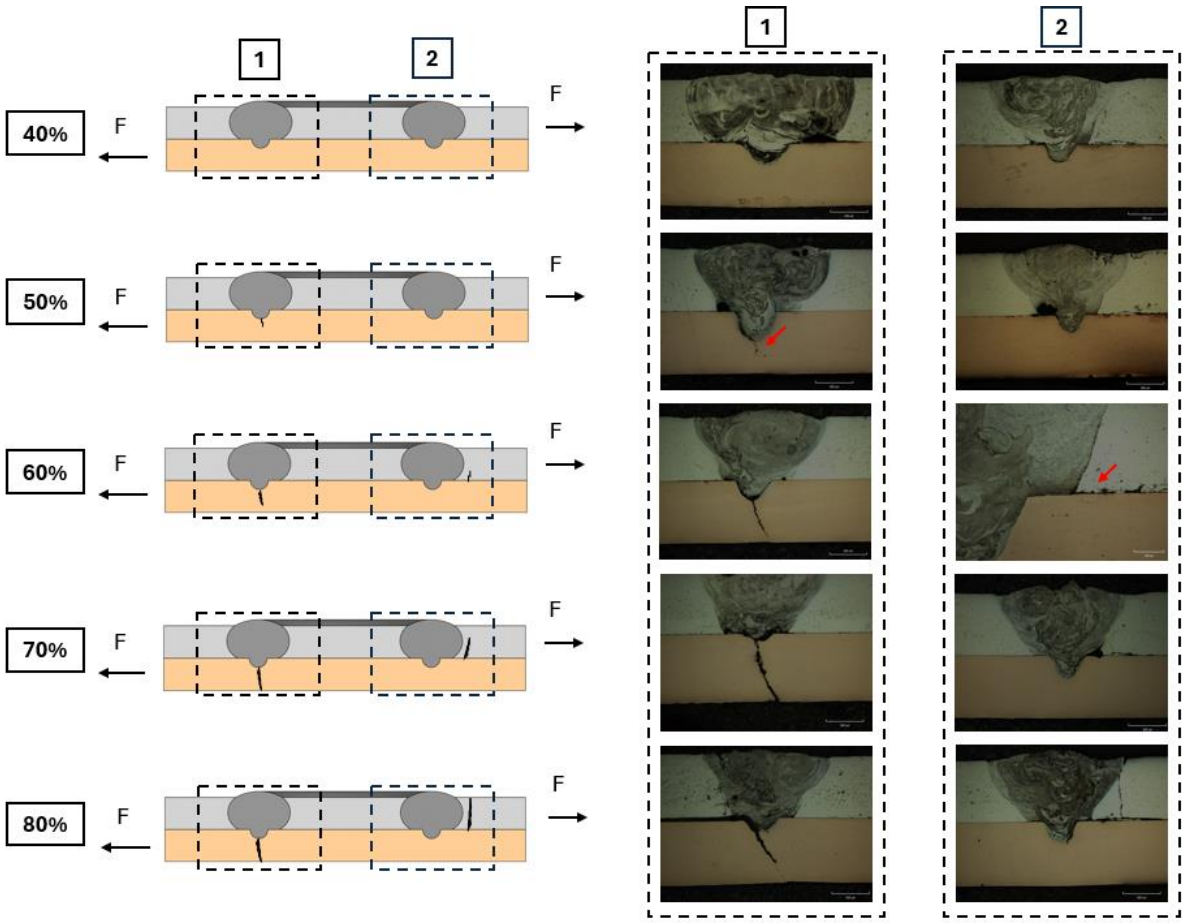



**Figure 38: Schematic representations and micrographs of cross-section (viewed along the dashed lines show in Figure 37) of the welds after interrupted tests at different stages of expected lives in 90° loading orientation**

The fatigue test matrix and corresponding load-life curve for the 67.5° loading orientation are presented in Table 10 and Figure 39, respectively. A total of 29 tests were conducted across 12 different load levels, with 2 to 3 replicates performed at each level. Low cycle fatigue was observed at 14,137 and 8,818 cycles for tests conducted at 85% of the peak quasistatic load, while runout was achieved at 43% of the peak quasistatic load. When comparing the fatigue test results between 90° and 67.5° loading orientation from Figure 40, it is evident that specimens tested at the 90° loading orientation generally exhibited a longer fatigue life for the same or similar load levels. This suggests that the pure shear conditions of the 90° loading orientation provide better resistance to fatigue compared to the 67.5° loading orientation, which subjects the welds to both shear and tensile stresses. The difference in fatigue performance becomes more noticeable at lower load levels, where specimens at 90° loading orientation achieved runout at a higher load level than those at 67.5°.

**Table 10: Test matrix for fatigue tests in 67.5° loading orientation with load levels determined from maximum load of quasistatic results and r-ratio = 0.1**

| Max. Load | Min. Load | Amp. | Freq. (Hz) | Test 1 | Test 2 | Test 3 |
|---|---|---|---|---|---|---|
| 0.43 | 0.043 | 0.162 | 10 | 2,000,000 | 1,361,148 | 2,000,000 |
| 0.45 | 0.045 | 0.201 | 10 | 1,909,280 | 1,652,619 | |
| 0.47 | 0.047 | 0.213 | 12 | 702,596 | 1,296,113 | 1,126,032 |
| 0.52 | 0.052 | 0.235 | 12 | 244,401 | 471,704 | 302,902 |
| 0.54 | 0.054 | 0.243 | 12 | 393,549 | 421,286 | |
| 0.57 | 0.057 | 0.256 | 15 | 130,644 | 332,803 | 240,451 |
| 0.60 | 0.060 | 0.269 | 15 | 204,224 | 179,882 | 273,174 |
| 0.62 | 0.062 | 0.277 | 15 | 156,310 | 155,439 | |
| 0.66 | 0.066 | 0.299 | 15 | 70,567 | 100,772 | |
| 0.71 | 0.071 | 0.320 | 15 | 47,795 | 74,776 | |
| 0.83 | 0.083 | 0.371 | 15 | 16,132 | 13,839 | |
| 0.85 | 0.085 | 0.38 | 15 | 8,818 | 14,137 | |

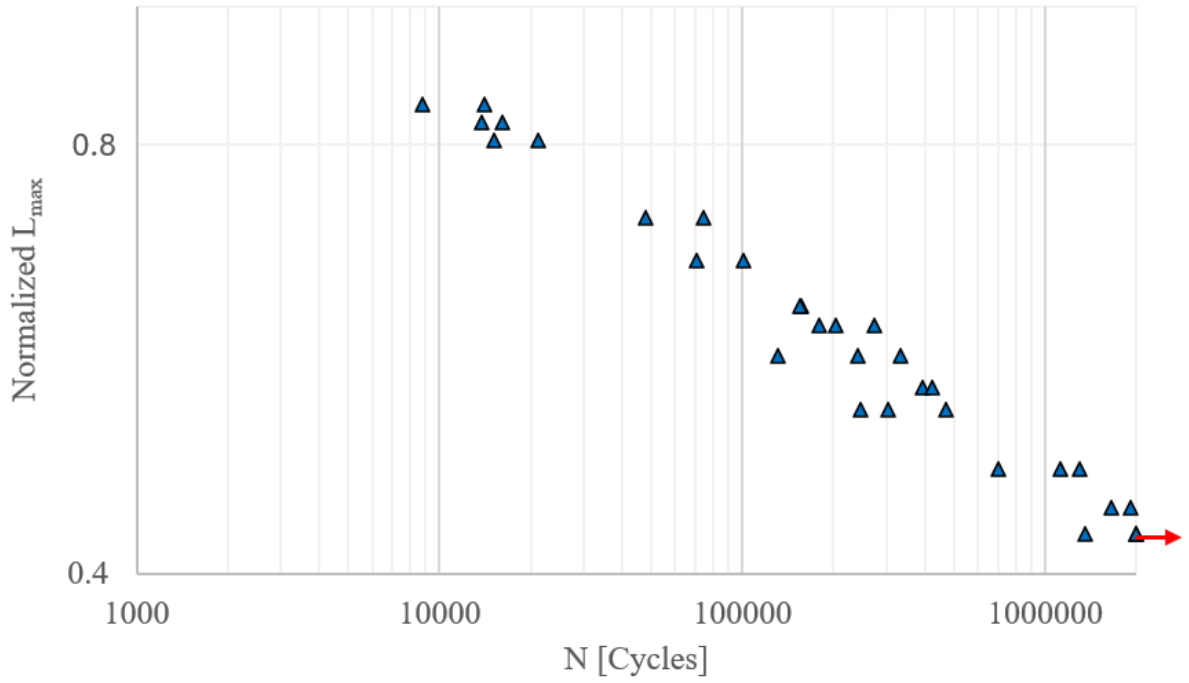



**Figure 39: Load-life curve for 67.5º loading orientation with arrow indicating runout data**

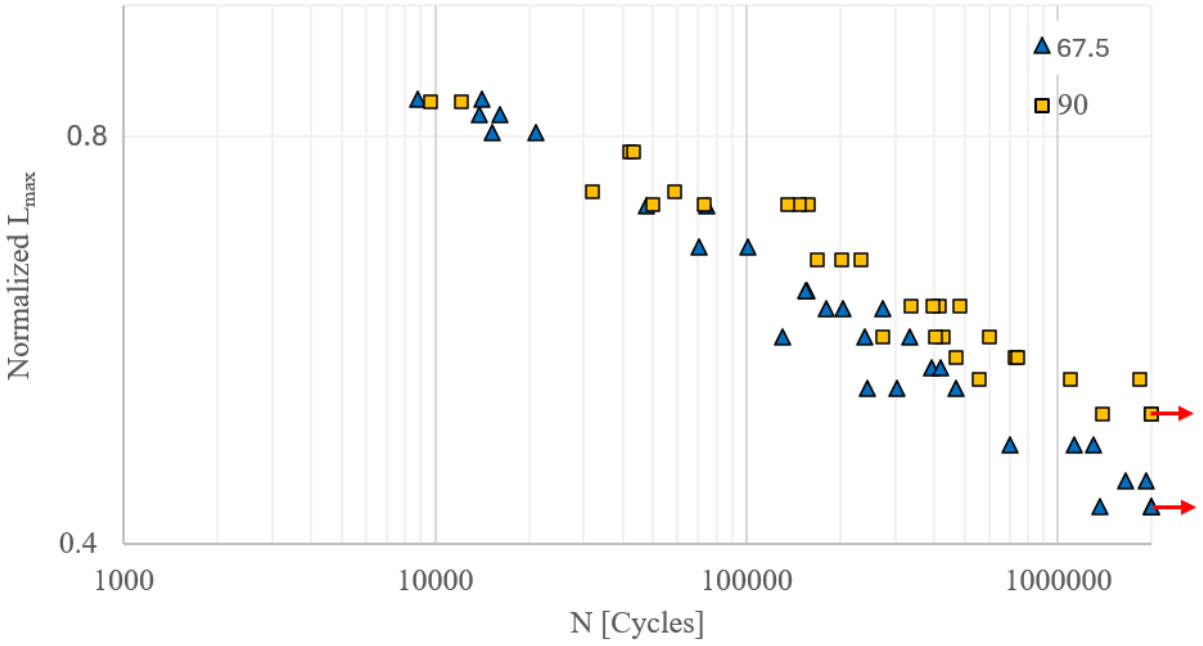



**Figure 40: Load-life curve for 90º and 67.5º loading orientations with arrows indicating runout data**

Although the 67.5º loading orientation is classified as biaxial, it is predominantly driven by shear forces. As a result, the observed failure mode closely resembled that of the 90º loading orientation, characterised by eyebrow failure. Figure 41 presents schematic representations and micrographs of the cross-sections of the welds obtained from an interrupted test at 70% of the expected life. It is evident that the crack on the copper side, which has also initiated at the weld root, has nearly fully propagated through the thickness of the copper sheet. Meanwhile, the crack on the aluminum side, which has initiated at the interface between the aluminum and copper sheets in the heat-affected zone, has propagated approximately one-third of the thickness of the aluminum sheet.

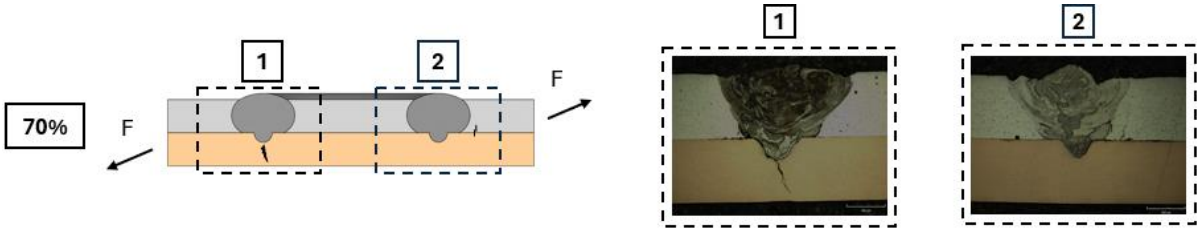
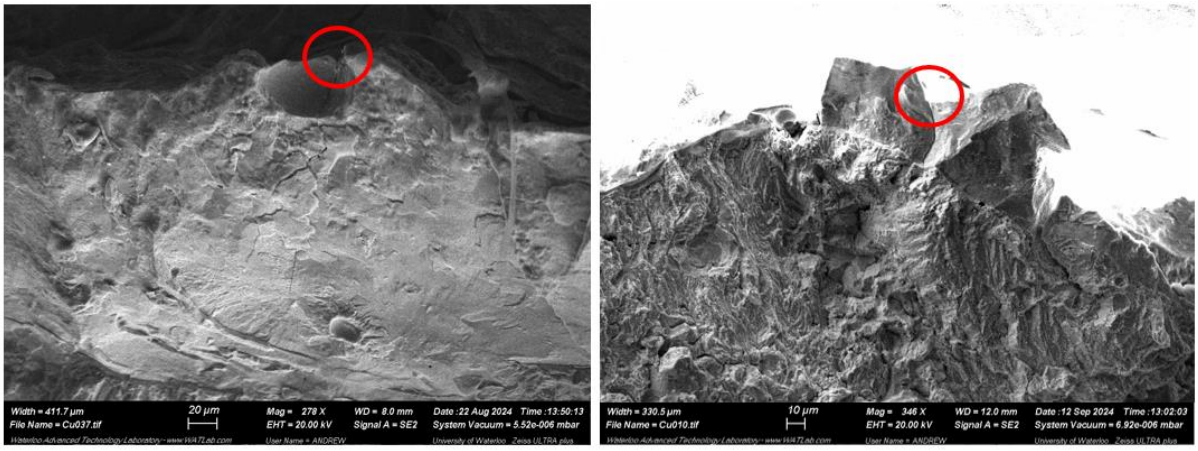



**Figure 41: Schematic representation and micrographs of cross-section of welds after interrupted test at 70% of expected life in 67.5º loading orientation**

During fatigue testing, since it was observed that the cracks initiated and propagated on the copper side first, further investigation into the fracture surface characteristics was performed. Instead of identifying a single distinct crack initiation site, multiple crack initiation sites were observed across all tested specimens. As illustrated in Figure 42, two primary mechanisms of crack initiation were identified: one at the porosity formed during the welding process and another at a sharp notch present at the weld root. These features act as stress concentration sites, significantly reducing fatigue strength of the weld. Additionally, the presence of brittle intermetallic compounds was identified as a major factor contributing to crack initiation. Figure 43 illustrates that EDS measurements reveal the existence of intermetallic compounds, primarily Al+$Al_2Cu$ and $Al_2Cu$, in the regions where cracks initiated. Although copper is generally harder and stronger than aluminum, the combined effects of stress concentrations at weld porosities and shar notches, along with the presence of intermetallic phases, create a failure mechanism that leads to the early initiation and propagation of fatigue cracks in the copper side of the weld joint.

.




(a) (b)

**Figure 42: Fracture surface on the copper side of the sample with 393,549 life, showing two types of crack initiation sites: (a) weld porosities (b) weld root notches**

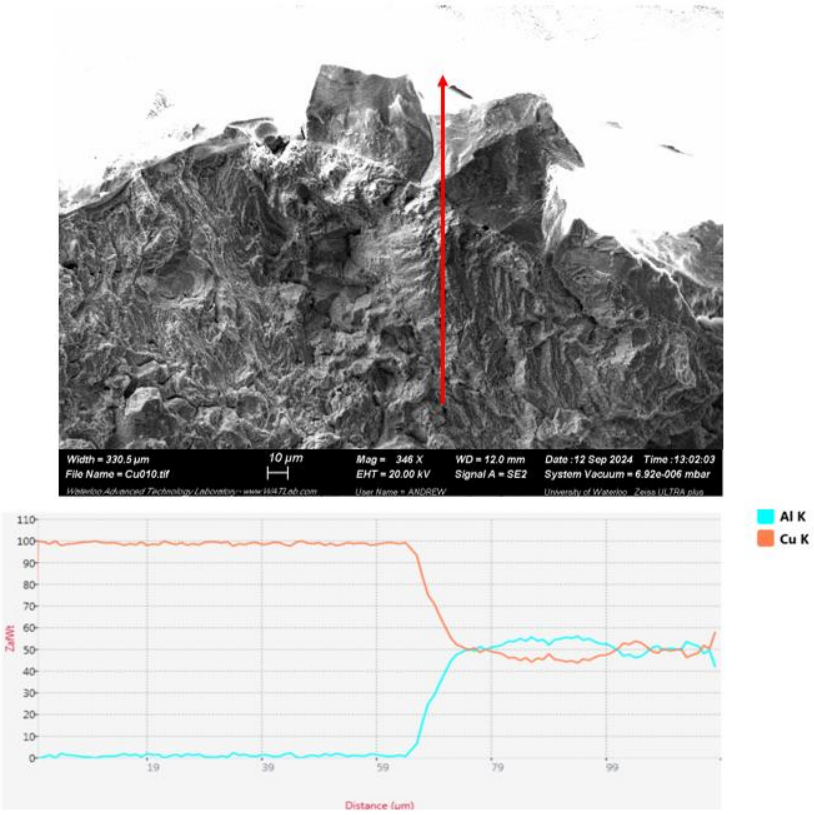



**Figure 43: EDS measurement at a crack initiation region (red arrow indicating direction of measurement)**

In the crack propagation region, distinct fatigue striations are clearly visible, as shown in Figure 44. The spacing between the striations increases progressively as the crack advances, indicating an acceleration in crack growth throughout the fatigue test. In the final fracture region, a relatively smooth fracture surface exhibits elongated dimples as seen in Figure 45. The presence of these elongated dimples is characteristic of ductile fracture, suggesting that the material experienced significant plastic deformation prior to failure.

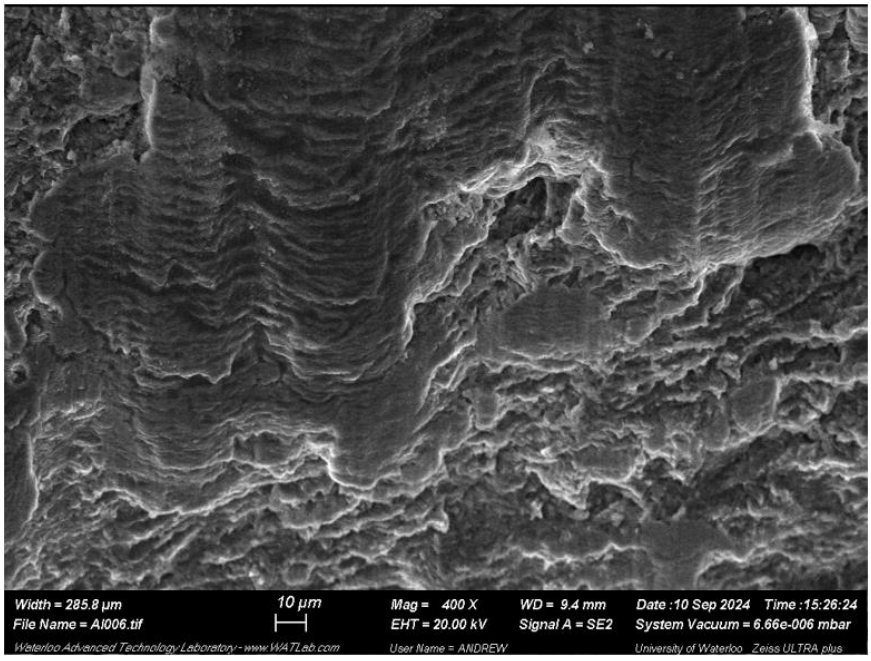



**Figure 44: Fracture surface on the copper side of the sample with 272,779 life, showing striations in the crack propagation region**

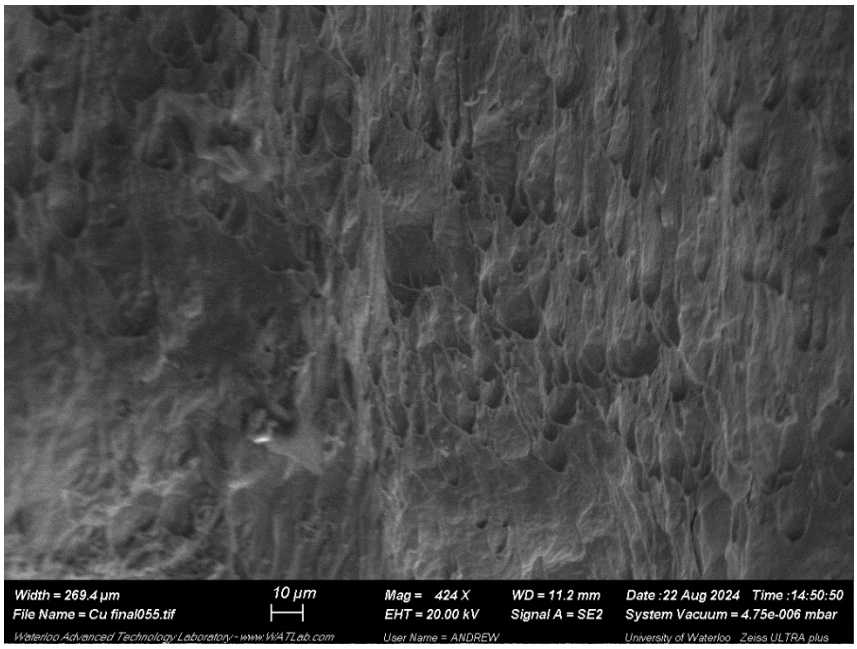



**Figure 45: Fracture surface on the copper side of the sample with 272,779 life, showing elongated dimples in the final fracture region**

# Chapter 5
# Fatigue Life Prediction

This chapter details the application of Rupp's model to Al-Cu laser welded joints. It thoroughly outlines the pre-processing and post-processing steps required to convert load-life data into stress-life plot. Additionally, statistical optimization is applied to further refine and collapse the stress-life data, resulting in the creation of a comprehensive master stress-life plot.

## 5.1 Rupp's Model Application to Cross-Tension Laser Welded Specimens

### 5.1.1 nCode Rupp's Model Pre-Processing

As discussed in section 2.5.2, the Al-Cu cross-tension laser weld specimen was modeled using the ACM method, following the guidelines provided by Joseph et al. [45]. The general modeling process is summarized in Figure 46. In this model, two S4R shell elements with a mesh size of 5 by 5 mm were employed to represent the aluminum and copper sheets. The upper and lower sheets were assigned 1100 aluminum (Young's modulus of 68.9 GPa and Poisson's ratio of 0.33) and 110 copper (Young's modulus of 117 GPa and Poisson's ratio of 0.34) properties respectively. Both shell elements were modeled with the same dimensions and orientation as those used in the actual cross-tension specimens. A C3D8 hexahedral solid element is employed to represent the weld nugget, and it was assigned 1100 aluminum properties, as the weld pool predominantly consists of aluminum. The hexahedral solid element is positioned between the upper and lower sheets at the actual weld location of the cross-tension specimen. Each node of the solid element is coupled to the shell nodes of the adjacent sheets through distributed coupling interpolation elements, where each patch consists of 4 elements as shown in Figure 46. The height of the solid element is defined by the gap between the sheets, which is equal to half the total sheet thickness, as the shell elements representing the sheets are positioned at their mid-planes as illustrated in Figure 47.

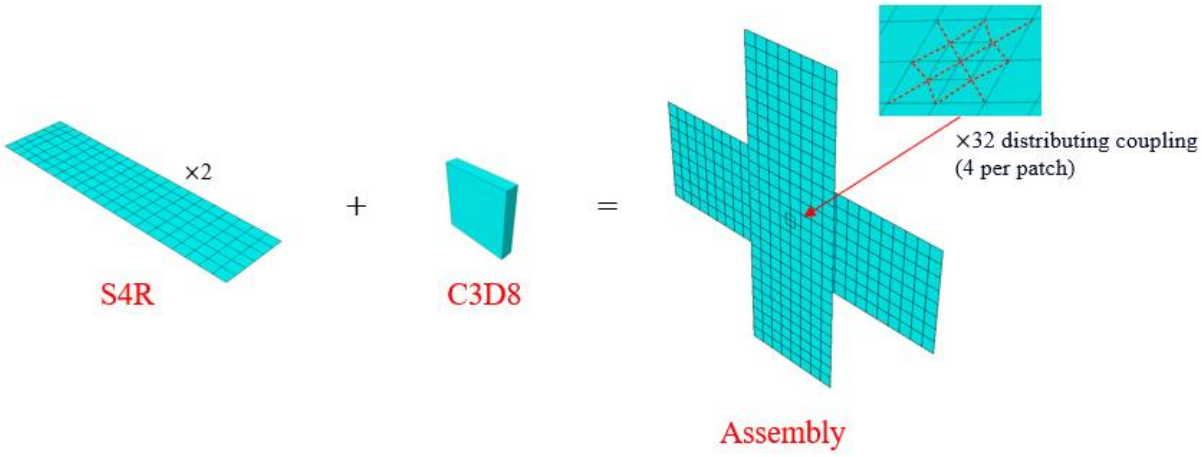



**Figure 46: Schematic representation of the ACM modeling process where red dashed lines represent the distributing coupling elements**

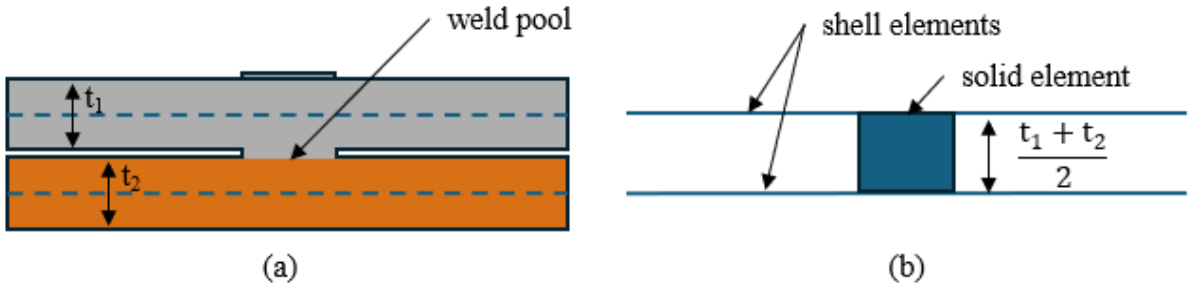



**Figure 47: Schematic representation of (a) al-cu laser weld (b) corresponding ACM model**

For both specimen configurations, the finite element model was oriented within the global coordinate system so that the z-axis aligns axially with the tubular geometry of the circular weld. This orientation ensures that the model accurately represents the loading conditions along the weld axis. The clamped areas on the left and right sides of the bottom (copper) shell element were fixed in all degrees of freedom to simulate the fixture clamping applied during the experimental process, as shown in Figure 48. The upper (aluminum) sheet was similarly constrained, with its two end areas connected to a reference point using beam-type multi-point constraints (MPCs), as illustrated in Figure 49. This reference point, positioned arbitrarily for modeling convenience, was constrained in all degrees of freedom except along the axis of loading. For a 90° loading orientation, the axis of loading is aligned with the x-axis, while

for a 67.5° loading orientation, the axis of loading involves a combination of the x- and z-axes, as shown in Figure 50, where the red arrows indicate the direction of applied loading.

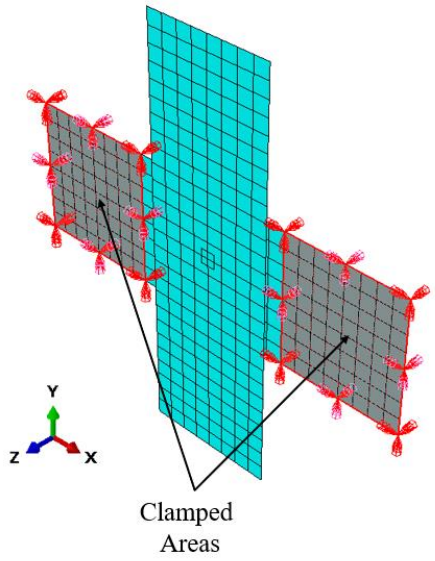



**Figure 48: Simplified finite element model of the cross-tension specimen highlighting two clamped areas of the bottom shell element**

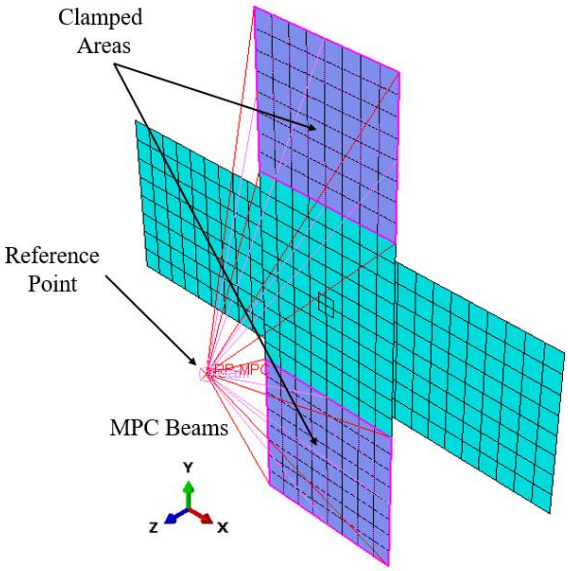



**Figure 49: Simplified finite element model of cross-tension specimen highlighting two clamped areas of the upper shell element**

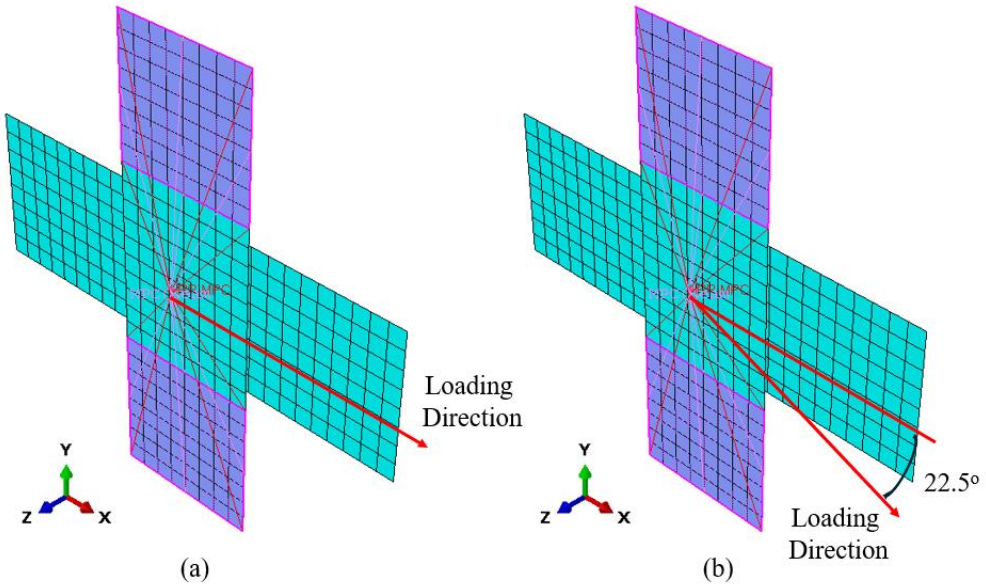



**Figure 50: Simplified finite element model of the cross-tension specimen highlighting load direction for (a) 90º loading orientation corresponding to Figure 31 and part (a) of Figure 32 (b) 67.5º loading orientation corresponding to part (b) of Figure 32**

### 5.1.2 nCode Rupp's Model Post-Processing

Since ABAQUS only allows for the extraction of nodal forces in global coordinates (with NFORC1, NFORC2, and NFORC3 field outputs), an additional transformation step, summarized in Figure 51, is required to transform these forces into local coordinate system. Following the procedure outlined in section 2.5.3, post-processing begins by extracting the stress components, $s_{11}$, $s_{12}$, $s_{13}$, $s_{21}$, …, $s_{33}$, from the C3D8 solid element in both the global and local coordinate systems. These components form the stress tensors $[T]$ and $[T']$, representing the stress state in the global and local systems, respectively. The next step involves calculating the eigenvectors of these stress tensors, denoted by $[P]$ and $[P']$, and sorted based on highest to the lowest eigen values, to capture the principal directions within each coordinate system. To ensure accuracy, an optional validation step can be conducted by confirming that the eigenvalues of the two stress tensors are the same or, in numerical terms reasonably close. Using these eigenvectors, the rotation matrix $[Q]$ is calculated following equation (7). This matrix defines the transformation necessary to relate the global coordinate system to the local one. Following the node numbering convention shown in Figure 52, the nodal forces $[F_n]$ for each node of the C3D8 solid element, are extracted in the global coordinate system. To obtain the nodal forces in local coordinates,

$[F_n']$, the rotation matrix $[Q]$ is applied according to equation (8), thereby transforming the global forces into their local equivalents.

$$[\boldsymbol{Q}] = [\boldsymbol{P}]^{-1} \times [\boldsymbol{P'}] \tag{7}$$

$$[\boldsymbol{F'_n}] = [\boldsymbol{Q}] \times [\boldsymbol{F_n}] \tag{8}$$

where $[\boldsymbol{F_n}] = \begin{bmatrix} \boldsymbol{F_{x,n}} \\ \boldsymbol{F_{y,n}} \\ \boldsymbol{F_{z,n}} \end{bmatrix}$ and $[\boldsymbol{F'_n}] = \begin{bmatrix} \boldsymbol{F'_{x,n}} \\ \boldsymbol{F'_{y,n}} \\ \boldsymbol{F'_{z,n}} \end{bmatrix}$ $\quad \boldsymbol{n = 1, 2, \dots, 8}$

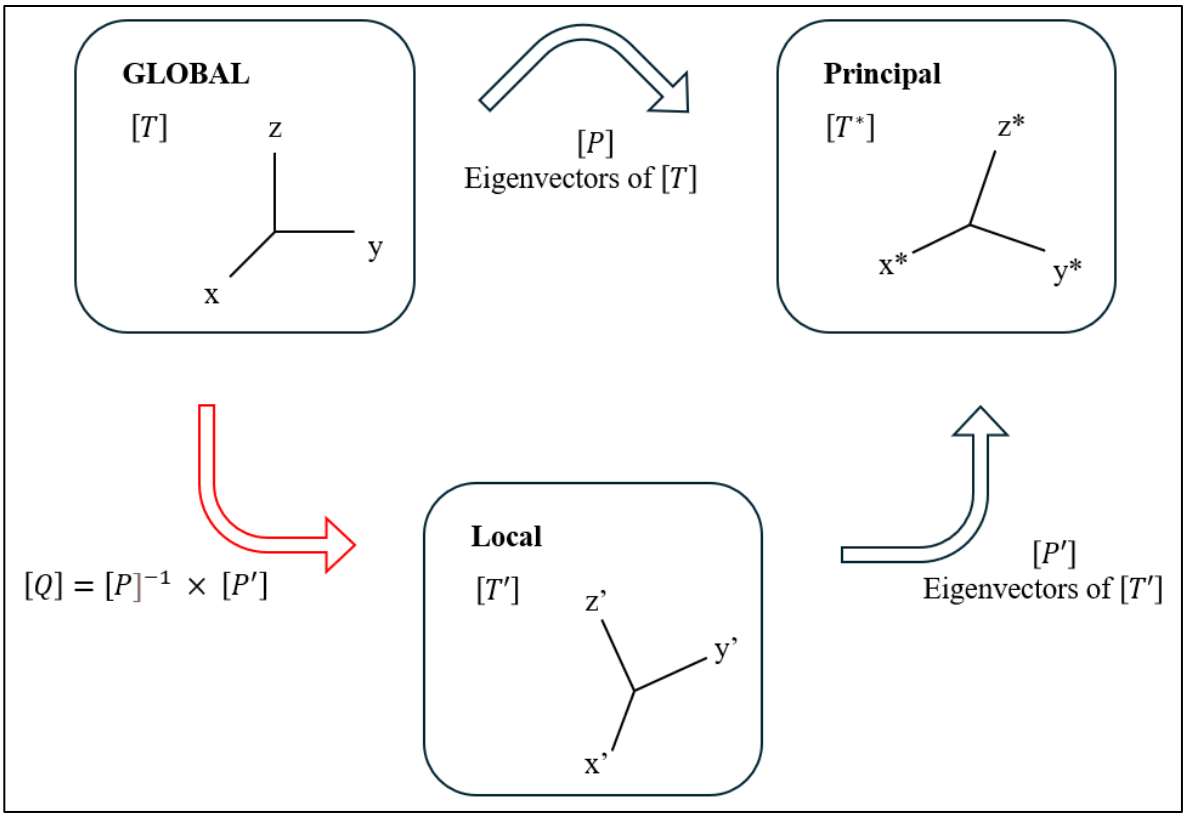



**Figure 51: Graphical representation of the rotation matrix calculation**

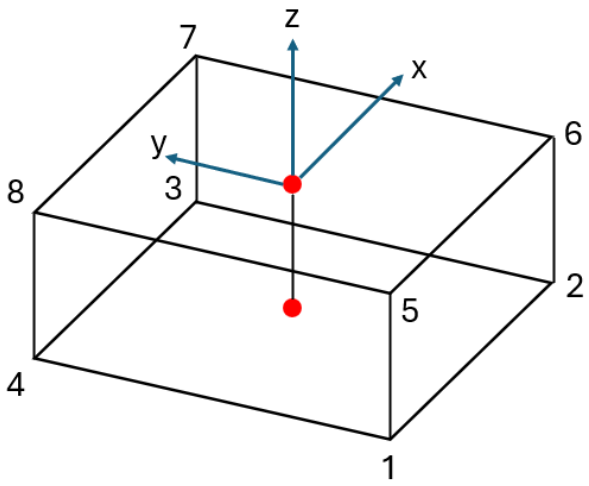



**Figure 52: Node numbers and coordinate system of the solid element**

For the top face, equivalent nodal forces at the center (highlighter by red points in Figure 52) are calculated using equations (10) – (12), while equivalent nodal moments at the center are calculated using equations (13) and (14). Similarly, equivalent nodal forces at the center of the bottom face are calculated using equations (15) – (17), and equivalent nodal moments at the center are calculated using equations (18) and (19). Since the copper sheet consistently failed in all fatigue tests, structural stress calculations are performed only for the bottom sheet. The calculated equivalent forces and moments for each load level are summarized in

Table 11. Using the values from Table 11, equations (1) – (6), and empirical factors typical of aluminum spot welds from Table 4, the corresponding structural stresses are calculated and presented in Table 12. Figure 53 displays the results after converting load-life data to stress-life data, showing a slight reduction in scatter compared to the load-life plot in Figure 40. While applying the spot weld life prediction model by Rupp et al., [32] modified by nCode with empirical factors for aluminum spot welds, helped collapse the fatigue data, the red lines in Figure 53 highlights room for further improvement in minimizing the error between predicted SSR and tested SSR.

$$\boldsymbol{F_{x,top}} = \sum_{\boldsymbol{i=5}}^{\boldsymbol{8}} \boldsymbol{F'_{x,i}} \tag{9}$$

$$\boldsymbol{F_{y,top}} = \sum_{\boldsymbol{i=5}}^{\boldsymbol{8}} \boldsymbol{F'_{y,i}} \tag{10}$$

$$\boldsymbol{F_{z,top}} = \sum_{\boldsymbol{i=5}}^{\boldsymbol{8}} \boldsymbol{F'_{z,i}} \tag{11}$$

$$\boldsymbol{M_{x,top}} = (\boldsymbol{F'_{z,5}} \cdot -\boldsymbol{L}) + (\boldsymbol{F'_{z,6}} \cdot -\boldsymbol{L}) + (\boldsymbol{F'_{z,7}} \cdot \boldsymbol{L}) + (\boldsymbol{F'_{z,8}} \cdot \boldsymbol{L}) \tag{13}$$

$$\boldsymbol{M_{y,top}} = (\boldsymbol{F'_{z,5}} \cdot \boldsymbol{L}) + (\boldsymbol{F'_{z,6}} \cdot -\boldsymbol{L}) + (\boldsymbol{F'_{z,7}} \cdot -\boldsymbol{L}) + (\boldsymbol{F'_{z,8}} \cdot \boldsymbol{L}) \tag{14}$$

$$\boldsymbol{F_{x,bottom}} = \sum_{\boldsymbol{j=1}}^{\boldsymbol{4}} \boldsymbol{F'_{y,j}} \tag{15}$$

$$\boldsymbol{F_{y,bottom}} = \sum_{\boldsymbol{j=1}}^{\boldsymbol{4}} \boldsymbol{F'_{y,j}} \tag{16}$$

$$\boldsymbol{F_{z,bottom}} = \sum_{\boldsymbol{j=1}}^{\boldsymbol{4}} \boldsymbol{F'_{z,j}} \tag{17}$$

$$\boldsymbol{M_{x,bottom}} = (\boldsymbol{F'_{z,1}} \cdot -\boldsymbol{L}) + (\boldsymbol{F'_{z,2}} \cdot -\boldsymbol{L}) + (\boldsymbol{F'_{z,3}} \cdot \boldsymbol{L}) + (\boldsymbol{F'_{z,4}} \cdot \boldsymbol{L}) \tag{18}$$

$$\boldsymbol{M_{y,bottom}} = (\boldsymbol{F'_{z,1}} \cdot \boldsymbol{L}) + (\boldsymbol{F'_{z,2}} \cdot -\boldsymbol{L}) + (\boldsymbol{F'_{z,3}} \cdot -\boldsymbol{L}) + (\boldsymbol{F'_{z,4}} \cdot \boldsymbol{L}) \tag{19}$$

where $\boldsymbol{L}$ is half of the distance from node 1 to 4

**Table 11: Calculated forces and moments for each load level**

| Loading Orientation [deg] | Max. Load | $F_x$ | $F_y$ | $F_z$ | $M_x$ | $M_y$ |
|---|---|---|---|---|---|---|
| 90 | 0.85 | 0.8491 | 0.0005 | -0.0110 | -1.03E-08 | 0.0003 |
| | 0.78 | 0.7794 | 0.0004 | -0.0093 | -9.74E-09 | 0.0003 |
| | 0.73 | 0.7293 | 0.0003 | -0.0081 | -9.28E-09 | 0.0003 |
| | 0.71 | 0.7123 | 0.0003 | -0.0078 | -9.12E-09 | 0.0003 |
| | 0.65 | 0.6494 | 0.0003 | -0.0064 | -8.50E-09 | 0.0003 |
| | 0.60 | 0.5993 | 0.0002 | -0.0055 | -7.97E-09 | 0.0002 |
| | 0.57 | 0.5695 | 0.0002 | -0.0050 | -7.66E-09 | 0.0002 |
| | 0.53 | 0.5295 | 0.0002 | -0.0043 | -7.21E-09 | 0.0002 |
| | 0.50 | 0.4997 | 0.0002 | -0.0038 | -6.92E-09 | 0.0002 |
| 67.5 | 0.85 | 0.7858 | -0.0004 | 0.3325 | 1.19E-07 | 0.0004 |
| | 0.82 | 0.7726 | -0.0003 | 0.2886 | 1.15E-07 | 0.0003 |
| | 0.71 | 0.6551 | -0.0002 | 0.2765 | 7.78E-08 | 0.0003 |
| | 0.66 | 0.6131 | 0.0000 | 0.2539 | 1.28E-08 | 0.0003 |
| | 0.62 | 0.5679 | -0.0002 | 0.2393 | 5.46E-08 | 0.0003 |
| | 0.60 | 0.5504 | -0.0002 | 0.2318 | 5.04E-08 | 0.0002 |
| | 0.57 | 0.5242 | -0.0002 | 0.2207 | 4.43E-08 | 0.0002 |
| | 0.54 | 0.4981 | -0.0001 | 0.2096 | 3.86E-08 | 0.0002 |
| | 0.52 | 0.4806 | -0.0001 | 0.2022 | 3.50E-08 | 0.0002 |
| | 0.47 | 0.4370 | -0.0001 | 0.1836 | 2.66E-08 | 0.0002 |
| | 0.45 | 0.4108 | -0.0001 | 0.1725 | 2.20E-08 | 0.0002 |
| | 0.43 | 0.3934 | -0.0001 | 0.1651 | 1.92E-08 | 0.0002 |

**Table 12: Calculated structural stresses for each load level**

| Loading Orientation [deg] | Max. Load | $\sigma_{max}(F_x)$ [MPa] | $\sigma_{max}(F_y)$ [MPa] | $\sigma_{max}(F_z)$ [MPa] | $\sigma_{max}(M_x)$ [MPa] | $\sigma_{max}(M_y)$ [MPa] | $\sigma_{sheet}$ [Mpa] |
|---|---|---|---|---|---|---|---|
| 90 | 0.85 | 13.0061 | 0.0073 | -0.0349 | -0.0011 | 37.1253 | 50.0965 |
| | 0.78 | 11.9380 | 0.0061 | -0.0294 | -0.0011 | 34.0756 | 45.9841 |
| | 0.73 | 11.1705 | 0.0053 | -0.0258 | -0.0010 | 31.8845 | 43.0293 |
| | 0.71 | 10.9113 | 0.0051 | -0.0246 | -0.0010 | 31.1443 | 42.0310 |
| | 0.65 | 9.9468 | 0.0042 | -0.0204 | -0.0009 | 28.3907 | 38.3171 |
| | 0.60 | 9.1793 | 0.0036 | -0.0174 | -0.0009 | 26.1998 | 35.3617 |
| | 0.57 | 8.7230 | 0.0032 | -0.0157 | -0.0008 | 24.8970 | 33.6043 |
| | 0.53 | 8.1111 | 0.0028 | -0.0136 | -0.0008 | 23.1502 | 31.2478 |
| | 0.50 | 7.6547 | 0.0025 | -0.0121 | -0.0008 | 21.8476 | 29.4902 |
| 67.5 | 0.85 | 12.0360 | -0.0054 | 1.0536 | 0.0132 | 39.7521 | 52.8417 |
| | 0.82 | 11.8350 | -0.0051 | 0.9145 | 0.0127 | 37.2695 | 50.0189 |
| | 0.71 | 10.0340 | -0.0038 | 0.8762 | 0.0086 | 32.9399 | 43.8500 |
| | 0.66 | 9.3912 | -0.0006 | 0.8046 | 0.0014 | 30.5403 | 40.7362 |
| | 0.62 | 8.6989 | -0.0029 | 0.7584 | 0.0061 | 28.4070 | 37.8643 |
| | 0.60 | 8.4314 | -0.0027 | 0.7346 | 0.0056 | 27.4998 | 36.6658 |
| | 0.57 | 8.0302 | -0.0025 | 0.6994 | 0.0049 | 26.1404 | 34.8700 |
| | 0.54 | 7.6298 | -0.0023 | 0.6641 | 0.0043 | 24.7848 | 33.0787 |
| | 0.52 | 7.3622 | -0.0021 | 0.6407 | 0.0039 | 23.8796 | 31.8825 |
| | 0.47 | 6.6937 | -0.0018 | 0.5819 | 0.0029 | 21.6208 | 28.8963 |
| | 0.45 | 6.2927 | -0.0016 | 0.5466 | 0.0024 | 20.2682 | 27.1075 |
| | 0.43 | 6.0259 | -0.0015 | 0.5232 | 0.0021 | 19.3698 | 25.9190 |

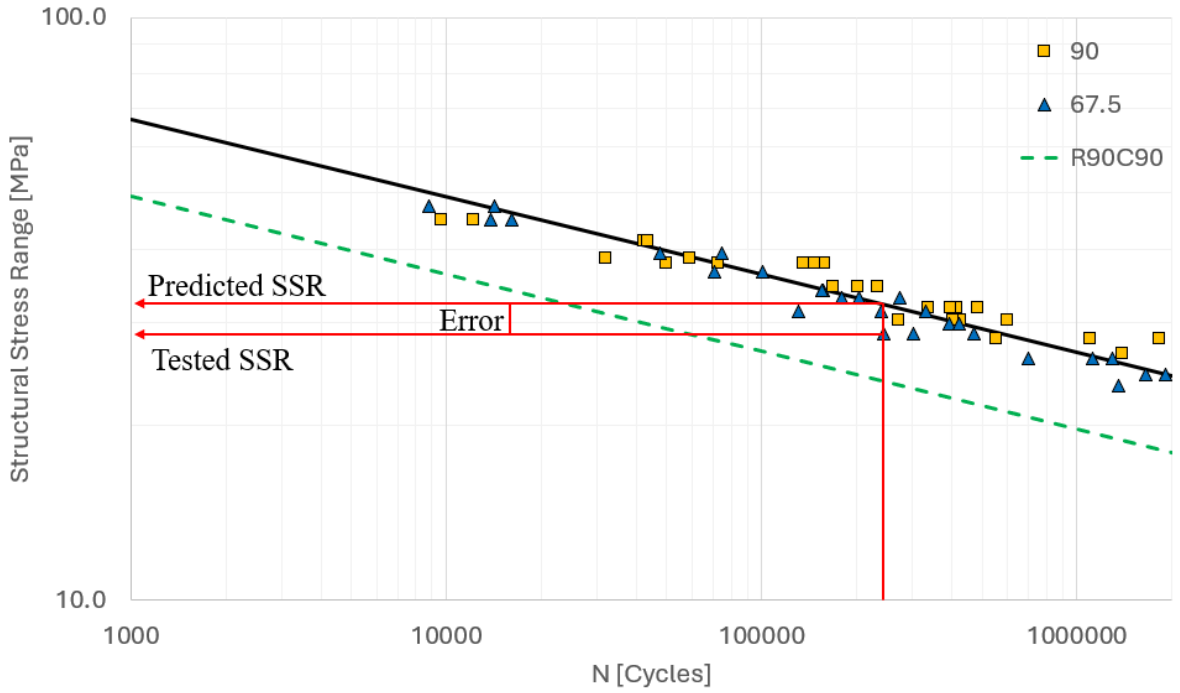



**Figure 53: Stress-life plot transferred from load-life using nCode aluminum RSW empirical factors**

An R90C90 curve was added to the fatigue data in Figure 53 (represented by the green dashed line) using the Owen tolerance limit method to establish a benchmark with 90% reliability at a 90% confidence level. This curve is constructed by calculating tolerance intervals that account for the standard deviation in the fatigue data, capturing the variability in fatigue life. By incorporating the standard deviation, this method defines a statistical boundary that compensates for data scatter, allowing for a reliable lower-bound threshold. Specifically, the interval is set below the mean fatigue life (indicated by the solid black line in Figure 53), forming a design curve that encompasses 90% of the population at a 90% confidence level.

## 5.2 Statistical Optimization

Data collapse in Figure 53 can be further optimized using the statistical method described in section 2.5.5, with the use of the nine empirical factors in equations (1) - (6). The optimization objective is to maximize the coefficient of determination, $R^2$, which ranges from 0 to 1, where a $R^2$ = 1 signifies a perfect fit with no errors in any data points. As equations (20) – (22) show, for a fixed data set, the total sum of squares ($SS_T$) remains constant; therefore, maximizing $R^2$ requires minimizing the sum of error

squares ($SS_E$). $SS_E$ represents the squared deviations between actual and predicted values, as illustrated in Figure 53, where, for instance, a specimen at a 67.5° loading orientation has an actual structural stress range of 28.69 MPa and a predicted range of 32.21 MPa.

$$\boldsymbol{R^2 = 1 - {SS_E}/{SS_T}} \tag{20}$$

$$\boldsymbol{SS_E = \sum_i (y_i - \hat{y}_i)^2} \tag{21}$$

$$\boldsymbol{SS_T = \sum_i (y_i - \bar{y})^2} \tag{22}$$

where $y_i$ and $\hat{y}_i$ represent the tested SSR and predicted SSR, respectively.

In this study, equation (20) is set as the objective function for the nonlinear generalized reduced gradient (GRG) method, applied to structural stress values for each of the 57 data points in Figure 53. Each structural stress term in the objective function includes an empirical factor from Table 4, which serves as a variable bounded within specified limits to achieve optimal results. Optimization is conducted using the nonlinear GRG solver available in Microsoft Excel, with empirical factor bounds set to ±1. The solution is considered converged when the change in the GRG becomes less than 0.0001 between iterations.

Figure 54 presents the results of non-linear generalized reduced gradient optimization for the Al-Cu laser weld fatigue data, where the $R^2$ value increased from 0.924 to 0.935. Although this improvement in $R^2$ does not appear significant, an additional measure of collapse performance is the change in percentage of data points within scatter bands. As shown in Figure 55, the proportion of data within the ±×2 scatter domain rose from 84% to 91%. The newly optimized empirical factors generated by the GRG optimization for Al-Cu laser welds with a circular weld seam are summarized in Table 13. It is important to note that since both loading orientations used to establish this model are shear-dominant, the model's reliability is particularly suited for applications with shear-dominant loading profiles.

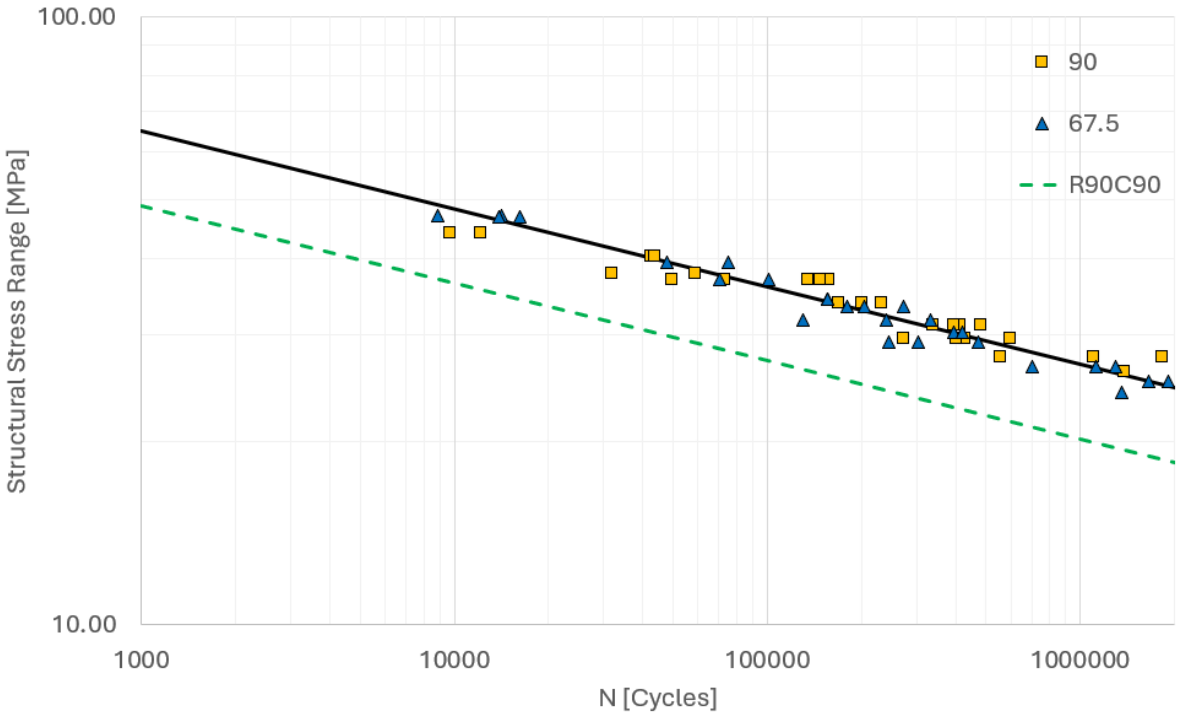



**Figure 54: Stress-life plot post statistical optimization**

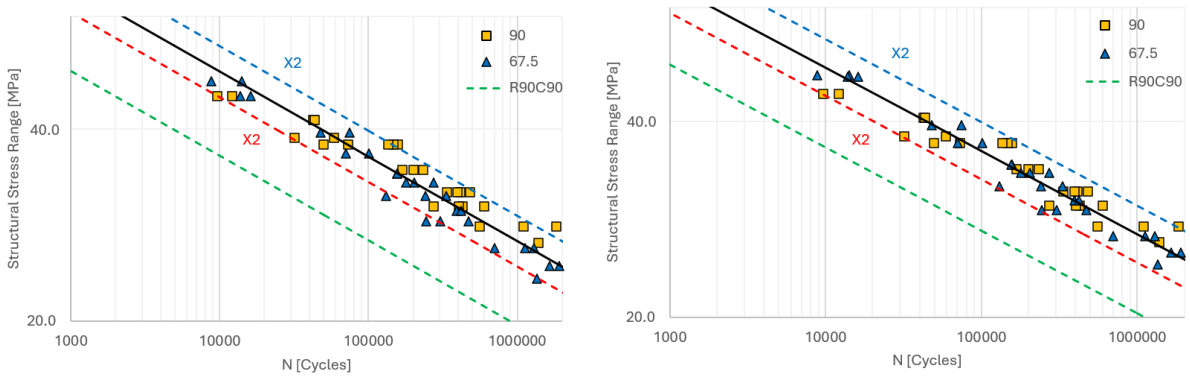



**Figure 55: Stress-life plot including ±×2 bands (a) pre statistical optimization (b) post statistical optimization**

**Table 13: Optimized empirical factors for Al-Cu laser welds with circular weld seams**

| Component | Factor | Diameter Exponent | Thickness Exponent |
|---|---|---|---|
| $F_x$, $F_y$ | SFFXY = 0.51 | DEFXY = 0.37 | TEFXY = -0.40 |
| $M_{x,}$ $M_y$ | SFMXY = -0.41 | DEMXY = 0.17 | TEMXY = -0.04 |
| $F_z$ | SFFZ = 1.00 | DEFZ = 0.81 | TEFZ = 0.10 |

## 5.3 Rupp's Model Validation

To validate the accuracy of the new prediction model with optimized parameters, five additional fatigue tests were performed: three at a 90° loading orientation under high-cycle fatigue conditions and two at a 67.5° loading orientation under low-cycle fatigue conditions. Table 14 summarizes the results for these additional load levels, including the corresponding structural stresses calculated using the optimized empirical factors. Figure 56 presents the resulting stress-life plot, which incorporates the new test data, demonstrating a strong alignment with the prediction model. As shown in Figure 57, the new data points fall well within the ±×2 scatter domain, further confirming the model's predictive reliability and suitability for various fatigue conditions.

**Table 14: Additional fatigue test results for model verification**

| Loading Orientation [deg] | Max. Load | Min. Load | Amp | Freq (Hz) | Test 1 | Test 2 | Test 3 | $\sigma_{sheet}$ [MPa] |
|---|---|---|---|---|---|---|---|---|
| 90 | 0.55 | 0.055 | 0.257 | 12 | 730,815 | 739,208 | 468,205 | 31.0985 |
| 67.5 | 0.81 | 0.081 | 0.363 | 15 | 21,092 | 15,212 | | 48.5490 |

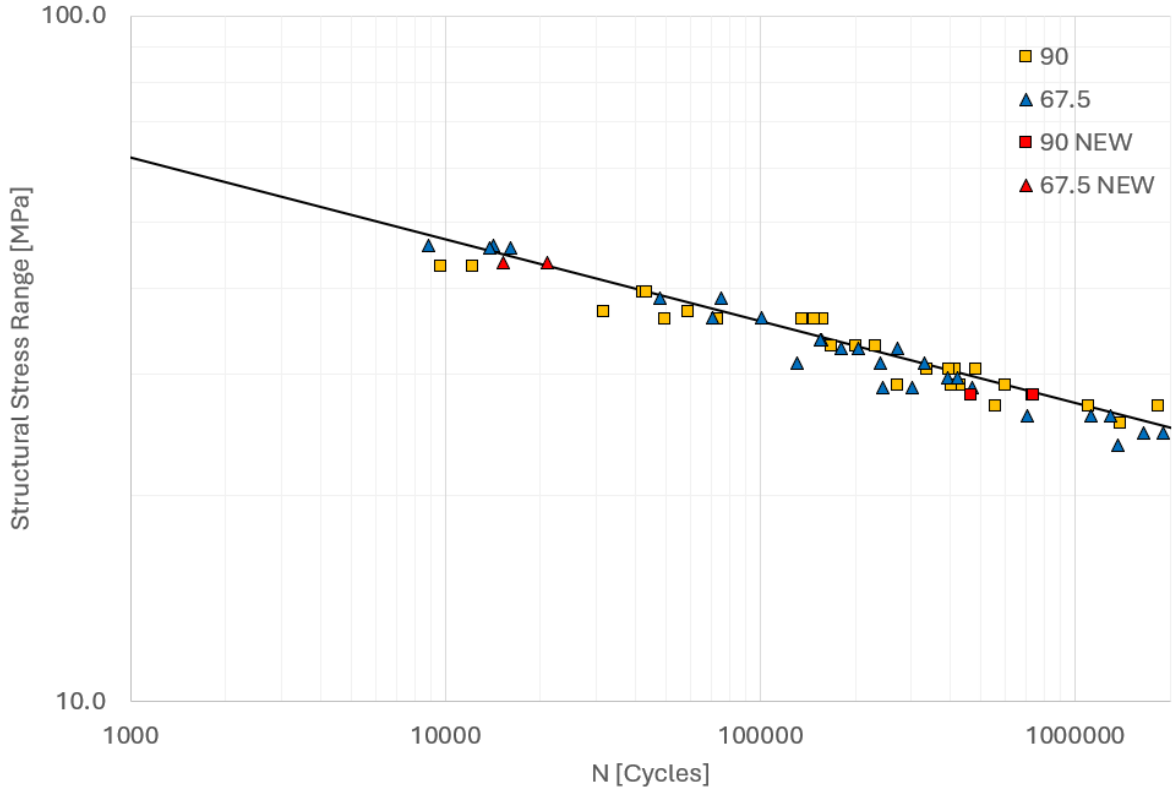



**Figure 56: Stress-life plot with additional test data for verification**

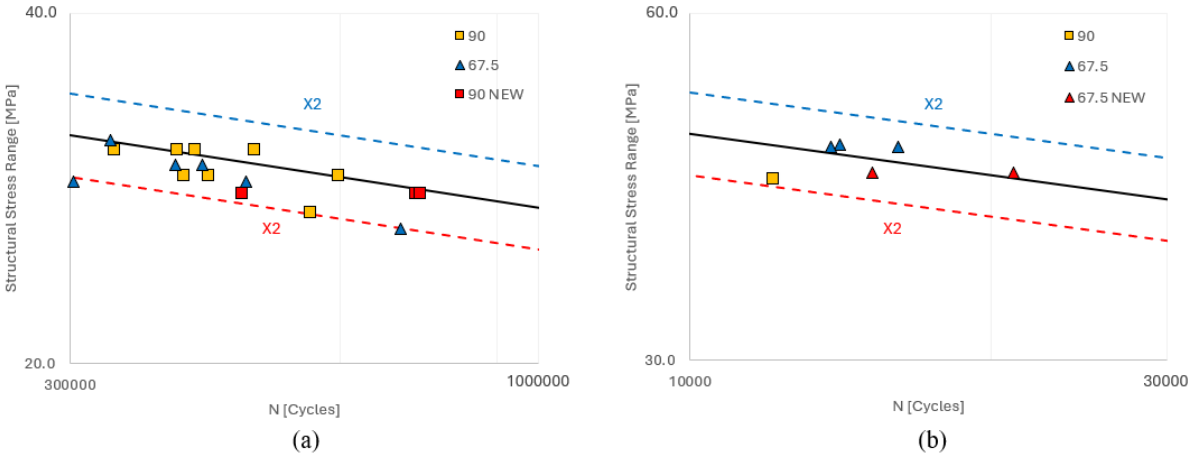



**Figure 57: Stress-life plot including ±×2 bands with additional test data in (a) 90º loading orientation (b) 67.5º loading orientation**

# Chapter 6
# Conclusions

## 6.1 Thesis Conclusions

The primary objective of this study was to support previous studies in assessing the feasibility of laser welding thin sheets of aluminum and copper and characterise the quasi-static and fatigue behavior of Al-Cu laser weld joints. Through a combination of experimental testing and modeling, this work provides valuable insights into the performance and durability of these dissimilar metal welds, which are critical in the design of electric vehicle battery packs. The contributions of this study are summarized as follows:

1. A comprehensive process window for both 0.6 mm and 0.3 mm laser spot sizes were developed through sensitivity analysis, covering a wide range of welding parameters to achieve robust Al-Cu laser weld joints. The optimal welding parameters were identified by selecting the combination of parameters that resulted in the highest tensile shear strength. Notably, the 0.3 mm spot size typically produced higher maximum shear forces compared to the 0.6 mm spot size.

2. Microstructural analysis using microhardness testing, SEM coupled with EDS, and XRD revealed two distinct regions of intermetallic compounds near the weld interface: Al+θ-$Al_2Cu$ and θ-$Al_2Cu$. These findings provide detailed insight into the formation and distribution of brittle phases, which play a significant role in joint durability.

3. Quasi-static and fatigue experiments on Al-Cu laser welded cross-tension specimens under shear-dominant loading orientations of $90^o$ and $67.5^o$ have been conducted and analyzed. When comparing the fatigue test results between the two loading orientations, specimens tested at the $90^o$ loading orientation generally exhibited a longer fatigue life for the same or similar load levels. Additionally, for both loading orientations, fatigue crack initiation occurred on the copper side of the weld interface, often at sites of porosity or sharp notches where intermetallic compounds were present.

4. The application of nCode Rupp's model to Al-Cu cross-tension laser welds allowed for the conversion of load-life data into stress-life plots, with a noticeable reduction in scatter. The model's predictive accuracy was further enhanced through statistical optimization using the GRG method, resulting in significant data collapse and improved scatter reduction.

5. Additional fatigue tests validated the predictive accuracy of the model, with new test data closely aligning with the stress-life plot. This confirms the model's reliability for shear-dominant loading conditions, establishing its suitability for fatigue life prediction across a range of loading profiles.

## 6.2 Recommendations and Future Work

Future research should prioritize refining laser welding parameters and exploring innovative techniques to mitigate the formation of brittle intermetallic compounds and reduce porosity and microcracks, thereby enhancing joint quality and durability. Approaches such as incorporating interlayers between aluminum and copper sheets, utilizing spatial beam oscillations, or implementing pulse-shaping techniques could significantly improve weld microstructure and fatigue resistance. To enhance applicability across broader operating conditions in an electric vehicle, future research could also examine the effects of power transmission, heat transfer, and different environmental factors, such as temperature variations, on the mechanical and electrical performance of the joints.

The predictive fatigue model developed in this study demonstrates strong capabilities; however, its accuracy is currently validated for shear-dominant loading conditions. Future work should extend the model to account for a wider range of loading orientations, including 45° and 0° configurations, which are relevant in real-world applications. Expanding the dataset to include diverse loading orientations, temperatures, and joint geometries would support the development of a more versatile model capable of accommodating complex loading scenarios typical in electric vehicle battery applications. Additionally, the integration of machine learning-based approaches could enhance model precision, offering a more accurate prediction of fatigue life.

# References


[1] A. Das, A. Barai, I. Masters, and D. Williams, “Comparison of tab-to-busbar ultrasonic joints for electric vehicle li-ion battery applications,” *World Electric Vehicle Journal*, vol. 10, no. 3, Sep. 2019, doi: 10.3390/wevj10030055.

[2] G. Esser, I. Mys, and M. H. Schmidt, “Laser micro welding of copper and aluminium using filler materials,” SPIE, Oct. 2004, pp. 337–342. doi: 10.1117/12.596330.

[3] S. Ali and J. Shin, “In-Depth Characterization of Laser-Welded Aluminum-and-Copper Dissimilar Joint for Electric Vehicle Battery Connections,” *Materials*, vol. 15, no. 21, p. 7463, Oct. 2022, doi: 10.3390/ma15217463.

[4] A. Das, D. Li, D. Williams, and D. Greenwood, “Joining Technologies for Automotive Battery Systems Manufacturing,” *World Electric Vehicle Journal*, vol. 9, no. 2, p. 22, Jul. 2018, doi: 10.3390/wevj9020022.

[5] V. Dimatteo, A. Ascari, E. Liverani, and A. Fortunato, “Experimental investigation on the effect of spot diameter on continuous-wave laser welding of copper and aluminum thin sheets for battery manufacturing,” *Opt Laser Technol*, vol. 145, p. 107495, Jan. 2022, doi: 10.1016/J.OPTLASTEC.2021.107495.

[6] M. F. R. Zwicker, M. Moghadam, W. Zhang, and C. V. Nielsen, “Automotive battery pack manufacturing – a review of battery to tab joining,” *Journal of Advanced Joining Processes*, vol. 1, p. 100017, Mar. 2020, doi: 10.1016/J.JAJP.2020.100017.

[7] H. Saariluoma, A. Piiroinen, A. Unt, J. Hakanen, T. Rautava, and A. Salminen, “Overview of optical digital measuring challenges and technologies in laser welded components in ev battery module design and manufacturing,” 2020, *MDPI*. doi: 10.3390/batteries6030047.

[8] P. Taheri, S. Hsieh, and M. Bahrami, “Investigating electrical contact resistance losses in lithium-ion battery assemblies for hybrid and electric vehicles,” *J Power Sources*, vol. 196, no. 15, pp. 6525–6533, Aug. 2011, doi: 10.1016/j.jpowsour.2011.03.056.

[9] L. N. Trinh and D. Lee, “The characteristics of laser welding of a thin aluminum tab and steel battery case for lithium-ion battery,” *Metals (Basel)*, vol. 10, no. 6, pp. 1–15, Jun. 2020, doi: 10.3390/met10060842.

[10] P. Schmalen, P. Plapper, I. Peral, I. Titov, O. Vallcorba, and J. Rius, “Composition and phases in laser welded Al-Cu joints by synchrotron x-ray microdiffraction,” in *Procedia CIRP*, Elsevier B.V., 2018, pp. 27–32. doi: 10.1016/j.procir.2018.08.006.

[11] A. Fortunato and A. Ascari, “Laser Welding of Thin Copper and Aluminum Sheets: Feasibility and Challenges in Continuous-Wave Welding of Dissimilar Metals,” *Lasers in Manufacturing and Materials Processing*, vol. 6, no. 2, pp. 136–157, Jun. 2019, doi: 10.1007/s40516-019-00085-z.

[12] M. J. Brand, P. A. Schmidt, M. F. Zaeh, and A. Jossen, “Welding techniques for battery cells and resulting electrical contact resistances,” *J Energy Storage*, vol. 1, no. 1, pp. 7–14, Jun. 2015, doi: 10.1016/J.EST.2015.04.001.

[13] S. S. Lee, T. H. Kim, S. J. Hu, W. W. Cai, and J. A. Abell, “Joining Technologies for Automotive Lithium-Ion Battery Manufacturing - A Review,” 2010. [Online]. Available: http://asmedigitalcollection.asme.org/MSEC/proceedings-pdf/MSEC2010/49460/541/2734863/541_1.pdf

[14] X. Cao, W. Wallace, C. Poon, and J. P. Immarigeon, “Research and progress in laser welding of wrought aluminum alloys. I. Laser welding processes,” *Materials and Manufacturing Processes*, vol. 18, no. 1, pp. 1–22, Jan. 2003, doi: 10.1081/AMP-120017586.

[15] D. Zuo, S. Hu, J. Shen, and Z. Xue, “Intermediate layer characterization and fracture behavior of laser-welded copper/aluminum metal joints,” *Mater Des*, vol. 58, pp. 357–362, Jun. 2014, doi: 10.1016/J.MATDES.2014.02.004.

[16] S. J. Lee, H. Nakamura, Y. Kawahito, and S. Katayama, “Effect of welding speed on microstructural and mechanical properties of laser lap weld joints in dissimilar Al and Cu sheets,” *Science and Technology of Welding and Joining*, vol. 19, no. 2, pp. 111–118, Feb. 2014, doi: 10.1179/1362171813Y.0000000168.

[17] H. S. Yoon and H. S. Bang, “The effect of wobbling on the welding characteristics in Al/Cu fiber laser welded joints,” *International Journal of Advanced Manufacturing Technology*, vol. 127, no. 11–12, pp. 5343–5352, Aug. 2023, doi: 10.1007/s00170-023-11653-1.

[18] S. Yan and Y. Shi, “Influence of laser power on microstructure and mechanical property of laser-welded Al/Cu dissimilar lap joints,” *J Manuf Process*, vol. 45, pp. 312–321, Sep. 2019, doi: 10.1016/J.JMAPRO.2019.07.009.

[19] J. Zhang, S. Guo, D. Wang, J. Xu, T. Huang, and R. Xiao, “Laser pressure welding of dissimilar aluminium and copper: microstructure and mechanical property,” *Science and Technology of Welding and Joining*, vol. 27, no. 1, pp. 52–60, 2022, doi: 10.1080/13621718.2021.2010449.

[20] T. Solchenbach and P. Plapper, “Mechanical characteristics of laser braze-welded aluminium–copper connections,” *Opt Laser Technol*, vol. 54, pp. 249–256, Dec. 2013, doi: 10.1016/J.OPTLASTEC.2013.06.003.

[21] T. Solchenbach, P. Plapper, M. Greger, J.-L. Biagi, J. Bour, and J. A. S. Bomfim, “Thermal and electrical aging of laser braze-welded aluminum–copper interconnects,” *Translational Materials Research*, vol. 1, no. 1, p. 015001, Jul. 2014, doi: 10.1088/2053-1613/1/1/015001.

[22] E. Huerta, A. I. Oliva, F. Avilés, J. González-Hernández, and J. E. Corona, “Elastic modulus determination of Al-Cu film alloys prepared by thermal diffusion,” *J Nanomater*, vol. 2012, 2012, doi: 10.1155/2012/895131.

[23] T. Solchenbach, P. Plapper, and W. Cai, “Electrical performance of laser braze-welded aluminum-copper interconnects,” *J Manuf Process*, vol. 16, no. 2, pp. 183–189, 2014, doi: 10.1016/j.jmapro.2013.12.002.

[24] P. Schmalen and P. Plapper, “Resistance measurement of laser welded dissimilar Al/Cu joints,” *Journal of Laser Micro Nanoengineering*, vol. 12, no. 3, pp. 189–194, Dec. 2017, doi: 10.2961/jlmn.2017.03.0003.

[25] I. Mys and M. Schmidt, “Laser micro welding of copper and aluminum,” in *Laser-based Micropackaging*, SPIE, Feb. 2006, p. 610703. doi: 10.1117/12.648376.

[26] M. M. Hailat, A. Mian, Z. A. Chaudhury, G. Newaz, R. Patwa, and H. J. Herfurth, “Laser micro-welding of aluminum and copper with and without tin foil alloy,” *Microsystem Technologies*, vol. 18, no. 1, pp. 103–112, Jan. 2012, doi: 10.1007/s00542-011-1378-8.

[27] V. Dimatteo, A. Ascari, and A. Fortunato, “Continuous laser welding with spatial beam oscillation of dissimilar thin sheet materials (Al-Cu and Cu-Al): Process optimization and

characterization," *J Manuf Process*, vol. 44, pp. 158–165, Aug. 2019, doi: 10.1016/J.JMAPRO.2019.06.002.

[28] K. Mathivanan and P. Plapper, "Laser welding of dissimilar copper and aluminum sheets by shaping the laser pulses," in *Procedia Manufacturing*, Elsevier B.V., 2019, pp. 154–162. doi: 10.1016/j.promfg.2019.08.021.

[29] M. Jarwitz, F. Fetzer, R. Weber, and T. Graf, "Weld seam geometry and electrical resistance of laser-welded, aluminum-copper dissimilar joints produced with spatial beam oscillation," *Metals (Basel)*, vol. 8, no. 7, Jul. 2018, doi: 10.3390/met8070510.

[30] W. J. Lai, S. J. Sung, J. Pan, Y. Guo, and X. Su, "Failure mode and fatigue behavior of dissimilar laser welds in lap-shear specimens of aluminum and copper sheets," *SAE International Journal of Materials and Manufacturing*, vol. 7, no. 3, pp. 706–710, 2014, doi: 10.4271/2014-01-1986.

[31] H. Jahed, B. Farshi, and M. Hosseini, "Fatigue life prediction of autofrettage tubes using actual material behaviour," *International Journal of Pressure Vessels and Piping*, vol. 83, no. 10, pp. 749–755, Oct. 2006, doi: 10.1016/J.IJPVP.2006.07.007.

[32] A. Rupp, K. Stijrzel, and V. Grubisic, "Computer Aided Dimensioning of Spot-Welded Automotive Structures."

[33] "DesignLife Theory Guide," 2013. [Online]. Available: www.hbm.com/ncode,

[34] H. T. Kang, X. Wu, A. K. Khosrovaneh, and Z. Li, "Data processing procedure for fatigue life prediction of spot-welded joints using a structural stress method," in *ASTM Special Technical Publication*, ASTM International, 2017, pp. 198–211. doi: 10.1520/STP159820160054.

[35] A. Tudor -George *et al.*, "New FEM Approach Including Technological Patterns for Automotive Spot Welding Parts," *Proceedings in Manufacturing Systems*, vol. 14, no. 4, pp. 163–168, 2019, [Online]. Available: https://www.researchgate.net/publication/363454850

[36] Dipl.-P. Daniel Heiserer, M. Chargin, and Dipl.-I. J. Sielaff, "High Performance, Process Oriented, Weld Spot Approach."

[37] K. M. Ragsdel and A. Asme, "The Generalized Reduced Gradient Method: A Reliable Tool for Optimal Design," 1977. [Online]. Available:

http://asmedigitalcollection.asme.org/manufacturingscience/article-pdf/99/2/394/6504539/394_1.pdf

[38] S. S. Rao, “Engineering Optimization Theory and Practice Fourth Edition.”

[39] P. Schmalen, P. Plapper, and W. Cai, “Process Robustness of Laser Braze-Welded Al/Cu Connectors,” *SAE International Journal of Alternative Powertrains*, vol. 5, no. 1, pp. 195–204, May 2016, doi: 10.4271/2016-01-1198.

[40] M. Weigl, F. Albert, and M. Schmidt, “Enhancing the Ductility of Laser-Welded Copper-Aluminum Connections by using Adapted Filler Materials,” *Phys Procedia*, vol. 12, no. PART 2, pp. 332–338, Jan. 2011, doi: 10.1016/J.PHPRO.2011.03.141.

[41] M. Akbari, R. Abdi Behnagh, and A. Dadvand, “Effect of materials position on friction stir lap welding of Al to Cu,” *Science and Technology of Welding and Joining*, vol. 17, no. 7, pp. 581–588, 2012, doi: 10.1179/1362171812Y.0000000049.

[42] E. Perez Zapico, A. Ascari, A. Fortunato, E. Liverani, and V. Dimatteo, “Influence of process parameters in blue laser welding of copper and aluminum thin sheets,” *J Laser Appl*, vol. 34, no. 4, Nov. 2022, doi: 10.2351/7.0000836.

[43] K. Lee *et al.*, “A study on cracks and IMCs in laser welding of Al and Cu,” *Manuf Lett*, vol. 35, pp. 221–231, Aug. 2023, doi: 10.1016/J.MFGLET.2023.08.026.

[44] J. Tian, W. Tao, and S. Yang, “Investigation on microhardness and fatigue life in spot welding of quenching and partitioning 1180 steel,” *Journal of Materials Research and Technology*, vol. 19, pp. 3145–3159, Jul. 2022, doi: 10.1016/j.jmrt.2022.06.083.

[45] S. Joseph, M. Hofmann, A. Schick, S. Joseph, and Dr.-I. A. Schick, “A mesh insensitive spot-weld model for improved fatigue life prediction A mesh insensitive finite element spot-weld model Development and verification.” [Online]. Available: https://www.researchgate.net/publication/280740285